ELSEVIER

Contents lists available at ScienceDirect

### Journal of Catalysis

journal homepage: www.elsevier.com/locate/jcat



## Computational and experimental insights into reactive forms of oxygen species on dynamic Ag surfaces under ethylene epoxidation conditions



Changming Liu <sup>a,1</sup>, Devinda P. Wijewardena <sup>b,1</sup>, Anna Sviripa <sup>a</sup>, Abinaya Sampath <sup>b</sup>, David W. Flaherty <sup>b,\*</sup>, Christopher Paolucci <sup>a,\*</sup>

#### ARTICLE INFO

# Article history: Received 31 August 2021 Revised 8 November 2021 Accepted 21 November 2021 Available online 26 November 2021

Keywords: (Ethylene Epoxidation Silver Density Functional Theory)

#### ABSTRACT

The partial oxidation of ethylene to ethylene oxide (EO) proceeds over supported Ag particles. Adsorption of molecular oxygen upon Ag forms the reactive oxygen species responsible for both epoxidation and combustion reactions, however, the catalyst surface structure and the molecular structure and identity of the reactive oxygen species present remain debated despite past use of appropriate forms of in situ spectroscopy. Specifically, there is no consensus for the molecular origin of widely reported Raman features that appear on contact with only O<sub>2</sub> or in reactant mixtures of C<sub>2</sub>H<sub>4</sub> and O<sub>2</sub> at pressures and temperatures relevant for the industrial process, in part, due to the lack of concerted ab initio studies that compute vibrational frequencies for oxygen-containing Ag surfaces. Here, we elucidate the molecular structure of the catalyst surface and reactive oxygen species by coordinating spectral deconvolution of transient and steady-state surface-enhanced Raman spectroscopy of Ag catalysts exposed to oxygen (2 - 101 kPa O<sub>2</sub>, 523 - 673 K) and mixtures of oxygen and ethylene (2 - 101 kPa O<sub>2</sub>, 0.5 - 9.8 kPa C<sub>2</sub>H<sub>4</sub>, 523 K) with ab initio thermodynamic modeling and vibrational frequency calculations. These comparisons suggest that during EO catalysis reconstructed surface oxides form and partially or completely encase metallic Ag particles. Raman features near 600 cm<sup>-1</sup> that persist in O<sub>2</sub> or cofed C<sub>2</sub>H<sub>4</sub> represent O-Ag-O structural motifs that form only on surface oxides and high oxygen-coverage reconstructed  $Ag_xO_y$  surfaces. We assign features centered near 810 - 840 cm<sup>-1</sup> and at higher frequencies, which are ubiquitous throughout the literature, to dioxygen complexes partially embedded within an oxide-like overlayer that forms during exposure either to O2 or during steady-state epoxidations. Taken together our results implicate the presence of a combination of monatomic and diatomic surface oxygen species, which emerge with appreciable quantities of subsurface oxygen at temperatures and O<sub>2</sub> pressures representative of EO catalysis.

© 2021 Elsevier Inc. All rights reserved.

#### 1. Introduction

Evolution of catalyst surface structure under reaction conditions, and recognition that the working state of the catalytic surface differs from that of a clean surface [1] were emphasized within the contributions of Michel Boudart [2,3]. Adsorbed molecules can saturate the catalyst surface, induce surface reconstructions [4-6], or form reactive overlayers [7-9]. These phenomena may manifest catalytically as reactions that are structure insensitive, an attribute Boudart recognized in 1966 [10] and subse-

quently reported several examples of that arise from disparate physical origins [11-14]. Boudart and Sajkowski later reviewed one such example of a structure insensitive reaction; the epoxidation of ethylene over Ag catalysts [13]. Areal rates of ethylene epoxidation under typical reaction conditions appear similar on different single crystal [15-17] and polycrystalline surfaces [18-20]. Analogously, *in situ* Raman spectroscopic measurements that interrogate the surface structure and reactive intermediates of different Ag ethylene epoxidation catalysts possess ubiquitous features [19], but the origin of these spectral features remains debated. In this contribution we employ spectral deconvolution of steady-state and transient Raman spectroscopy integrated with quantum chemical calculations to provide insights into the structure of the Ag catalyst surface and reactive forms of oxygen under ethylene epoxidation reaction conditions.

<sup>&</sup>lt;sup>a</sup> Department of Chemical Engineering, University of Virginia, Charlottesville, VA 22903, United States

<sup>&</sup>lt;sup>b</sup> Department of Chemical and Biomolecular Engineering, University of Illinois Urbana-Champaign, Illinois 61801, United States

<sup>\*</sup> Corresponding authors.

E-mail addresses: dwflhrty@illinois.edu (D.W. Flaherty), cp9wx@virginia.edu (C. Paolucci)

<sup>&</sup>lt;sup>1</sup> These authors contributed equally.

Industrially, ethylene oxide (EO) is produced by reactions of oxygen and ethylene upon Ag catalysts, promoted with multiple chemical species (Cl, alkaline and other metals [21-28]) and supported on  $\alpha$ -Al<sub>2</sub>O<sub>3</sub> at temperatures between 473 and 573 K [29] and with reactant feeds consisting of either a stoichiometric excess of C<sub>2</sub>H<sub>4</sub> to O<sub>2</sub> [21] or excess of O<sub>2</sub> to C<sub>2</sub>H<sub>4</sub> [19,30]. The mechanism involves competing pathways that include a selective pathway that forms EO and a non–selective pathway that creates acetaldehyde, which combusts subsequently to yield H<sub>2</sub>O and CO<sub>2</sub>. Despite this chemistry being extensively studied [19], the detailed mechanism and molecular structure of the reactive oxygen species that form under epoxidation conditions remain debated.

Different hypotheses aim to describe the nature of oxygen species on Ag and explain the drastic effects of oxygen coverage on EO formation rates and selectivities. On metallic unreconstructed Ag surfaces at low coverages of oxygen, studies agree that EO and combustion products form by a series of elementary steps that dissociatively adsorb O2, molecularly adsorb C2H4, and transfer atomic O\* to C2H4\* to form oxametallacycles (OMC) that react further to evolve the epoxide or acetaldehyde [31-44]. In contrast, a smaller body of computational work by van Santen and colleagues used Ag<sub>2</sub>O (001) surfaces [32,33,35-37,45] or metallic slabs with subsurface oxygen [46] as a model representation for the active state of the Ag catalyst, which had been proposed to resemble a Ag-oxide layer. Density functional theory (DFT) calculations on Ag<sub>2</sub>O (001) suggested that EO forms by direct reaction between C<sub>2</sub>H<sub>4</sub> (g) and lattice O-atoms, and acetaldehyde forms (and subsequently combusts) when ethylene reacts at oxygen vacancies on Ag<sub>2</sub>O (001).

Van Santen et al. approached EO catalysis with a perspective inspired by earlier work of Cant and Hall [47], Sachtler [48], Kuipers [49], van den Hoek [46], Campbell [15,16,50-52], and Lambert [17,53,54], which proposed that the surface and subsurface of the active catalyst possessed high contents of O-atoms. Specifically, EO forms with higher selectivities on Ag surfaces with significant amounts of surface and subsurface O-atoms [55]. These high oxygen coverages form a reconstructed surface oxide [56-61]. Moreover. Ag and O-atoms move dynamically in these structures [18,56,62] at temperatures relevant for EO production ( $\sim$ 473 – 573 K) [29]. Subsurface oxygen atoms increase the selectivity to EO along with the oxidation state of catalytically accessible Ag atoms, which creates increasingly electrophilic O\*-atoms on the surface [16,18,48,50,53,54,63,64]. X-ray photoelectron spectroscopy (XPS) shows multiple types of O\*-atoms present on Ag surfaces [64-66], and ex situ coverages of the more electrophilic form of O\*-atoms (O 1 s at > 530 eV) often show a positive correlation with selectivities to EO [67]. Overall, higher O-atom contents in the surface and subsurface increase the fraction of oxygen that is electrophilic, which favors epoxidation of the C=C bond over abstraction of H-atoms and subsequent combustion [44,68]. Taken together, these studies suggest that the mechanism and selectivity for EO formation depend sensitively on the types of oxygen species that form on the surface and subsurface of Ag under reaction

Surface-enhanced Raman scattering (SERS) accesses the vibrational frequencies required to directly probe atomic oxygen and reconstructed oxide layers on Ag surfaces and has been extensively used to examine the features that form following  $O_2$  activation and adsorption [55,59,61,69-80]. Similar peaks attributed to oxygen species are consistently observed near  $\sim$  250, 350, 600, 800 and 950 cm $^{-1}$  on both polycrystalline and single crystal Ag surfaces. Notably, the commonly observed feature near 800 cm $^{-1}$  diminishes upon exposure to gas mixtures containing ethylene but persists during steady-state reaction [59], which suggests the corresponding form of surface oxygen exists in a pool of reactive

species that participate in catalysis. While assignments in the literature for features below 600 cm $^{-1}$  contain some discrepancies, these peaks are frequently attributed to v(Ag-O) modes of atomic oxygen present at low-coverages upon Ag surfaces or beneath the plane of the outer most monolayer of Ag. In contrast, discussions of the molecular structures responsible for the high wavenumber ( $\sim$ 600 – 1000 cm $^{-1}$ ) bands have not reached consensus with researchers proposing that such features may reflect forms of atomic or diatomic oxygen present on surfaces and debating the roles (direct or indirect) these intermediates hold for ethylene epoxidation [19].

Despite decades of research, the Ag surface structure under reaction conditions and molecular origin of these Raman bands remains debated, in part due to a dearth of computational studies that connect vibrational frequencies to molecular structures on Ocontaining Ag surfaces. Here, we elucidate the molecular structure of the catalyst surface and reactive O-species by coordinating spectral deconvolution of transient and steady-state SERS measurements of Ag catalysts exposed to oxygen and mixtures of oxygen and ethylene with ab initio thermodynamic modeling and vibrational frequency calculations. Experimental and computational results together demonstrate that at oxygen and ethylene compositions relevant for EO catalysis, surfaces of Ag reconstruct to form an oxide film that encapsulates a metallic core. These reconstructions change the thermodynamic stabilities of reactive forms of oxygen present upon surfaces and favor significant coverages of diatomic oxygen species. Recognition of this state of the catalyst surface can reconcile the molecular identity of O-species in frequently observed Raman features and suggests that the observed structure insensitivity of ethylene epoxidation may be a consequence of surface reconstruction and formation of an oxide-like overlayer.

#### 2. Materials and methods

#### 2.1. Materials and material preparation

Polycrystalline Ag nanoparticles (US Research Nanomaterials, 99.99%) with diameters in the range of 80 – 100 nm were used in Raman spectroscopy experiments. The reported synthesis method of these particles forms a layer of organic ligand upon the surface of the nanoparticles [81], which is removed by *in situ* thermal treatments. Samples of Ag<sub>2</sub>O (Sigma-Aldrich, ReagentPlus, 99%) were used as standards for comparisons of X–ray diffraction patterns.

#### 2.2. Catalyst characterization

The crystallinity of bulk Ag nanoparticles as received and following specified oxidative and reductive thermal treatments were determined using an X-ray diffractometer (XRD, Bruker, D8 Advance). Powder XRD patterns were obtained from 20 values of  $5^{\circ}$  to  $100^{\circ}$  using Cu K $\alpha$  radiation (0.15418 nm) under ambient conditions. Known literature sources were used to identify the diffraction features of these nanoparticles.

#### 2.3. In situ Raman spectroscopy

Raman spectroscopy was performed on Ag nanoparticles in contact with reactant gases using a Raman spectrometer (Renishaw, InVia) equipped with a charged-couple detector (CCD) and using 532 nm laser adjusted to deliver low power densities at the sample (0.025 – 0.25 mW  $\mu m^{-2}$ ). The laser power at the sample stage was measured directly with a power meter. (Gentec-EO, PRONTO-SI).

All spectra were obtained with a long 50X objective and using a cell designed for *in situ* measurements within reactive environments (Linkam CCR1000,  $\sim$ 5 cm³ volume) equipped with a quartz window. Reported spectra reflect coadded measurements acquired over periods of 1 – 5 s in transient measurements or for 30 s for measurements at steady-state. Spectra were collected with a resolution of  $\sim$  1.5 cm $^{-1}$ , and the accuracy of the reported features is judged to be similar based upon calibrations performed using the 520 cm $^{-1}$  feature of a Si (111) wafer.

The Ag nanoparticles were formed into aggregates (pellets) by applying high pressures (3.4 – 4.9 MPa) for 5 – 10 min using a pellet press (Carver, Model C) to produce structures with a cross-sectional area of  $\sim 4~\rm mm^2$  and a thickness of  $\sim 1~\rm mm$ . These aggregates were loaded into the crucible of the *in situ* cell and oxidatively pretreated with the intent to remove all carbonaceous surface residues and to roughen the surface. Standard conditions for the pretreatment were heating typically to 523 K (101 kPa  $O_2$ , 523 K, 4 h), although a temperature of 673 K was used where noted. Spectra obtained from Ag samples treated in this manner and using a 532 nm laser possess high signal to noise ratios due to surface-enhanced Raman scattering (SERS) [59,72].

The steady-state experiments were performed using a range of combinations of the pressures of  $C_2H_4$  (0.5 -  $\sim$ 9.8 kPa  $C_2H_4$ ) (Air-Gas, 10% C<sub>2</sub>H<sub>4</sub>, balance He, primary standard custom mix), and  $O_2$  (2 – 80 kPa  $O_2$ , AirGas, 99.99%) at a total pressure of  $\sim 101$  kPa across the range of temperatures from 423 K to 673 K. At each composition, spectra were acquired continuously for periods up to 3 h in duration. In situ Raman spectra no longer changed following 1.5 h at each combination of reactant pressure and temperature, which demonstrated that these measurements represent the steady-state structure of the operating Ag catalyst and the corresponding coverages of surface intermediates. Spectra were obtained from the top surface of a packed catalyst bed, therefore, the composition of the gas corresponds to the composition of the feed stream controlled by the mass flow controllers. Consequently, readsorption of products (e.g., ethylene oxide, water) were negligible.

Transient Raman experiments were performed as follows. Raman spectra were taken at a fixed temperature while the compositions of the flowing gas were changed periodically from oxidative (101 kPa O<sub>2</sub>, AirGas, 99.99%) to reductive (101 kPa H<sub>2</sub>, AirGas, 99.999%) conditions in repeating cycles typically 2 h in length.

Multi-variate curve resolution alternating least squares (MCR-ALS) analysis (details in **Section S.1**) methods were used to extract principal components of spectra that may be representative of surface and subsurface intermediates [82] acquired from spectra obtained at steady-state within different combinations of reactants (i.e., differences in  $O_2$  and  $C_2H_4$  pressures) but also for time-resolved measurements that sought to capture the transient oxidation or reduction of the Ag catalysts following step changes in pressures of  $O_2$ ,  $H_2$ , and  $C_2H_4$ .

#### 2.4. Density functional theory calculations

We performed DFT calculations with the Vienna Ab initio Simulation Package (VASP version 5.4.4) [83] and the GGA-PBE [84] exchange–correlation functional. All calculations were non-spin-polarized and used a plane wave cutoff energy of 400 eV and the projector augmented wave (PAW) method for core-valence interactions [85,86]. Bulk fcc Ag (Fm $\bar{3}$  m) and Ag<sub>2</sub>O (Pn $\bar{3}$  m) structures were taken from the Materials Project database [87], and their geometries and cell vectors were subsequently optimized using  $10^{-8}$  eV and 0.01 eV/Å for energy and force convergence criteria, respectively. The k-points and lattice parameters used for bulk Ag and Ag<sub>2</sub>O are reported in **Section S.2**.

#### 2.4.1. Surface calculations for $Ag_xO_y$ structures

The asymmetric  $Ag_xO_y$  slabs proposed in literature (vide infra) were generated through the Atomic Simulation Environment (ASE) [88] and Python Materials Genomics (pymatgen) [89] codes. Additionally, for each Ag facet we sampled surfaces with O adsorbed on symmetrically unique sites [90,91] at coverages varying from 0.06 to 0.83 monolayers (ML). For the  $Ag_xO_y$  calculations, we used the k-point density from the k-points per reciprocal Å for Ag bulk in the x and y directions (rounded up), and a single k-point in the z direction. At least 12 Å of vacuum was added for all surface calculations. Surfaces were optimized to convergence criteria of  $10^{-8}$  eV and 0.01 eV/ Å. All slabs were asymmetric and had at least four layers of Ag atoms, with the two bottom layers fixed. We calculated harmonic vibrational frequencies (parallelized using ASE [88]) for surfaces by numerical differentiation of atomic forces with 0.015 Å displacements and an energy convergence criterion of 10<sup>-8</sup> eV. For Ag<sub>2</sub>O<sub>3</sub> frequency calculations, only the top two to three layers in the structures were displaced, so that the calculations were more efficient while the local environment of surface O was kept undisturbed. Here, we define surface O-atoms as those whose nuclei lie above that for the outermost layer of Ag atoms, and subsurface O as those atoms with nuclei that reside below those of the outermost layer of Ag atoms.

#### 2.4.2. Ab initio thermodynamics

To relate calculated  $Ag_xO_y$  energies to experimental conditions, we used *ab initio* thermodynamics to compute free energies [92]:

$$\gamma \left( T, p_{O_2} \right) = \frac{1}{A} \left( E_{\rm DFT} - E_{\rm ref} - N_{\rm Ag} \mu_{\rm Ag} - N_{\rm O} \mu_{\rm O}(T, p_{O_2}) \right) \tag{1}$$

where  $\gamma$  is the Gibbs free energy, A and  $E_{\rm DFT}$  are the surface area and total energy of the  ${\rm Ag_xO_y}$  slab, respectively,  $E_{\rm ref}$  is the total energy of the Ag slab,  $N_{\rm Ag}$  is the difference in the number of Ag in the  ${\rm Ag_xO_y}$  slab compared to the Ag slab,  $N_{\rm O}$  is the number of oxygen atoms in the  ${\rm Ag_xO_y}$  slab,  $\mu_{\rm O}$  is the chemical potential of oxygen, and  $\mu_{\rm Ag}$  is the chemical potential for Ag, which we define as the energy of an Ag atom in the Ag bulk structure. We related  $\mu_{\rm O}$  to the pressure of  ${\rm O_2}$  (g) as follows:

$$\mu_{0}(T, p_{0_{2}}) = \frac{1}{2} (E_{0_{2}} + \mu_{0_{2}}(T) + kT \ln(\frac{p_{0_{2}}}{p^{\circ}}))$$
 (2)

$$\Delta\mu_{\rm O}(T,p_{\rm O_2}) = \mu_{\rm O}(T,p_{\rm O_2}) - \frac{1}{2}E_{\rm O_2} \eqno(3)$$

Here,  $E_{\rm O_2}$  is the calculated energy of an isolated O<sub>2</sub> molecule,  $\mu_{\rm O_2}$  is calculated using the NIST JANAF Thermochemical tables [93], and  $p^{\circ}$  is the pressure at standard state (101 kPa).

#### 3. Results and discussion

## 3.1. Crystallographic structure of Ag nanoparticles before and following thermal treatments

To determine the bulk structure of Ag nanoparticles under reaction conditions, we collected XRD patterns following exposure to  $O_2$  or mixtures of  $O_2$  and  $C_2H_4$ . Fig. 1 shows XRD patterns from Ag and Ag $_2O$  materials following distinct thermal treatments. The diffractogram for as-received Ag $_2O$  possesses XRD peaks corresponding to the (111), (200), (220), and (311) planes of Ag $_2O$ , along with less intense peaks for the (110), (222), (400), (331) and (420) planes. The as-received Ag nanoparticles show XRD features characteristic of bulk Ag with prominent peaks corresponding to the (111), (200), (220) and (311) planes with lower intensity features corresponding to (222) and (400) planes. The XRD patterns of Ag nanoparticles following oxidative treatments

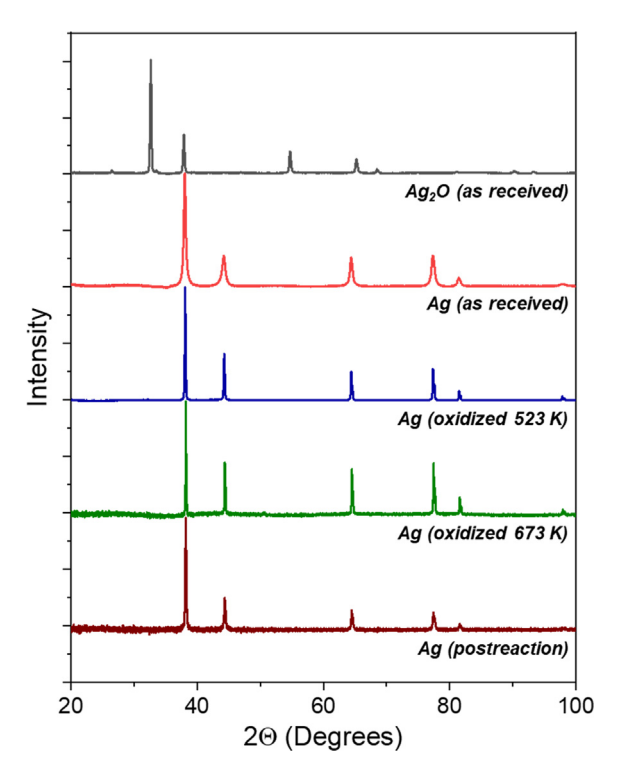


**Fig. 1.** X-Ray diffractograms of as-received bulk  $Ag_2O$  (black), as received Ag nanoparticles (red), Ag nanoparticles following oxidative treatment at 523 K (20 kPa  $O_2$ , 5 h; blue), pelletized Ag nanoparticles following oxidative treatments at 673 K (101 kPa  $O_2$ , 673 K, 3 h; green), and pelletized Ag nanoparticles following *in situ* Raman experiments.

at lower (20 kPa O<sub>2</sub>, 81 kPa N<sub>2</sub>, 523 K, 5 h) and higher temperatures (101 kPa O<sub>2</sub>, 673 K, 3 h) resembles that of the as received Ag nanoparticles [94-96]. Furthermore, these features remain largely unchanged following reactions with C<sub>2</sub>H<sub>4</sub> and O<sub>2</sub> (0.5 - 9.8 kPa  $C_2H_4$ , 2 – 80 kPa  $O_2$ , 523 K for 2 h, see Fig. 1) for a duration of at least 24 h most strongly resemble those of bulk Ag. These thermal treatments result in a shift of the feature for the (111) plane to slightly higher angles (38.0° to 38.2°) and a decrease in the full width half maximum of this feature, which signify the elimination of lattice defects and an increase in the mean crystallite diameter as a consequence of thermal annealing. Significantly, diffraction features representative of Ag<sub>2</sub>O domains are undetectable within XRD patterns of initial Ag nanoparticles following oxidative treatments (523 or 673 K) and following catalysis. These comparisons demonstrate that Ag nanoparticles do not form sufficiently large or ordered domains of Ag<sub>2</sub>O. Nanoparticles of Ag dissociatively adsorb and bind oxygen with coverages that exceed a monolayer on contact with O2 and during ethylene epoxidation in stoichiometric excesses of oxygen [65,97], which suggests the O\*-atoms reside near surfaces in disordered structures or structures of length scales insufficient to provide coherent diffraction. While such structures evade detection by XRD, surface enhanced Raman spectroscopy reveal their presence and how they depend on the pressure of C<sub>2</sub>H<sub>4</sub> and O<sub>2</sub> reactants during catalysis (vide infra).

#### 3.2. In situ Raman spectra during Steady-State ethylene epoxidation

Silver surfaces and nanoparticles form ethylene oxide when contacted with  $O_2$  and  $C_2H_4$  reactants at temperatures between 473 and 573 K [20,48,51,70,98]. Fig. 2 shows steady-state Raman spectra acquired at distinct combinations of  $O_2$  and  $C_2H_4$  pressures at 523 K (Fig. 2a, 2 kPa  $O_2$ , 0.5 – 9.8 kPa  $C_2H_4$ ; Fig. 2b, 2 kPa  $C_2H_4$ , 2

- 80 kPa O<sub>2</sub>). These spectra remain representative spectra over periods of multiple hours during which spectral features maintain constant lineshape and intensity demonstrating that the catalyst achieved steady-state surface structures and coverages. Fig. 2a shows a prominent asymmetric feature at 810 cm<sup>-1</sup> with a shoulder near 910 cm $^{-1}$  along with smaller peaks at  $\sim$  350 cm $^{-1}$ , 990 cm $^{-1}$  and 1050 cm $^{-1}$  at the lowest  $C_2H_4$  pressure (0.5 kPa C<sub>2</sub>H<sub>4</sub>). The most intense feature shifts to lower wavenumbers ( $\sim$ 812 cm<sup>-1</sup>, 1 kPa C<sub>2</sub>H<sub>4</sub>) and subsequently vanishes as ratios of [C<sub>2</sub>H<sub>4</sub>] to [O<sub>2</sub>] increase and then exceed unity. The disappearance of the  $\sim 810~\text{cm}^{-1}$  peak correlates with the attenuation of peaks at  $\sim 350~\text{cm}^{-1},\,990~\text{cm}^{-1}$  and  $1050~\text{cm}^{-1}$  and the appearance of a broad band centered between 600 and 640 cm<sup>-1</sup>. The changes occur also with intensification of a peak at  $\sim 220~\text{cm}^{-1}$ , a shoulder near  $\sim 520~\text{cm}^{-1}$ , and the emergence of an asymmetric peak at  $980 \text{ cm}^{-1}$  and broad features at  $1340 \text{ cm}^{-1}$  and  $1590 \text{ cm}^{-1}$ . The intensity of peaks above 1250 cm<sup>-1</sup> become more significant with increases in [C<sub>2</sub>H<sub>4</sub>]. Several of the peaks that emerge between 750 and 1300 cm<sup>-1</sup> with increasing [C<sub>2</sub>H<sub>4</sub>] have been assigned to vibrational modes of EO and are discussed in detail below [41,70,98-1001.

Fig. 2b shows Raman spectra collected at varying  $[O_2]$  (2 – 80 kPa  $O_2$ , 2 kPa  $C_2H_4$ ) at 523 K, which illustrate the evolution of spectral features at higher  $[O_2]$  to  $[C_2H_4]$  ratios. The trends in the growth and attenuation of Raman active features as functions of the ratio of  $[O_2]$  to  $[C_2H_4]$  agree with those in Fig. 2a, which suggests these surfaces are saturated with  $O_2$ – and  $C_2H_4$ –derived intermediates and have a negligible number of unoccupied sites. Features at 220, 350, 810, 910, and 990 cm<sup>-1</sup> decrease in intensity as the ratio of  $[C_2H_4]$  to  $[O_2]$  increases (both Fig. 2a and Fig. 2b). These peaks are most intense under the most strongly oxidizing conditions (i.e., highest  $[O_2]$  to  $[C_2H_4]$  ratios, Fig. 2b), which coincides with attenuation of the broad band with a peak at 600 – 640 cm<sup>-1</sup>. The changes suggest that the prior features correspond to forms of  $O_2$ –derived surface intermediates.

The response of the Raman features to reactant pressures (Fig. 2) give strong evidence that different forms of oxygen species coexist with organic species on the Ag catalyst surface at  $[C_2H_4]$  to  $[O_2]$  ratios and temperatures (473 K – 573 K) commonly used for industrial ethylene epoxidation [19,101,102]. Based on prior investigations utilizing infrared [70,98,99], high-resolution electron energy loss [41], and Raman [76-78] spectroscopy to characterize the surface species formed upon contact of  $O_2$ ,  $C_2H_4$ , or  $C_2H_4O$  with Ag nanoparticles or single crystal surfaces, we consider assignments for the features shown in Fig. 2.

Table 1 summarizes the Raman bands shown in Fig. 2 and peak assignments reported previously for experiments performed either with systems containing only O2 and Ag or from spectroscopy performed during ethylene epoxidation, coadsorption of C<sub>2</sub>H<sub>4</sub> and O<sub>2</sub>, or low temperature adsorption of C<sub>2</sub>H<sub>4</sub>O. Features associated only with distinct forms of oxygen and Ag nanoparticles or surfaces include a number of assignments. Bands near 220 cm<sup>-1</sup> were previously assigned to Ag-O stretching modes of either atomic or diatomic oxygen on silver surfaces. Peaks at  $\sim 350~\text{cm}^{-1}$  are consistently assigned to the v(Ag-O) mode of atomic oxygen species. The band near 600 cm<sup>-1</sup> has conflicting assignments to either stretching modes of bulk O,  $\nu(Ag-O_{bulk})$ , subsurface O,  $\nu(Ag-O_{sub-})$ surface) or diatomic O  $v(Ag-O_2)$ . The asymmetric feature that extends from 810 to 910 cm<sup>-1</sup> encompasses a range of prior observations with contradictory assignments of surface and subsurface atomic and diatomic oxygen. At higher frequencies, the 990 cm<sup>-1</sup> corresponds to either atomic or diatomic oxygen upon Ag surfaces.

Past work also describes features attributed to organic surface species formed in the presence of both  $C_2H_4$  and reactive oxygen species or by direct adsorption of  $C_2H_4O$ , which include chemisorbed ethylene ( $C_2H_4^*$ ) and ethylene oxide ( $C_2H_4O^*$ ) but also car-

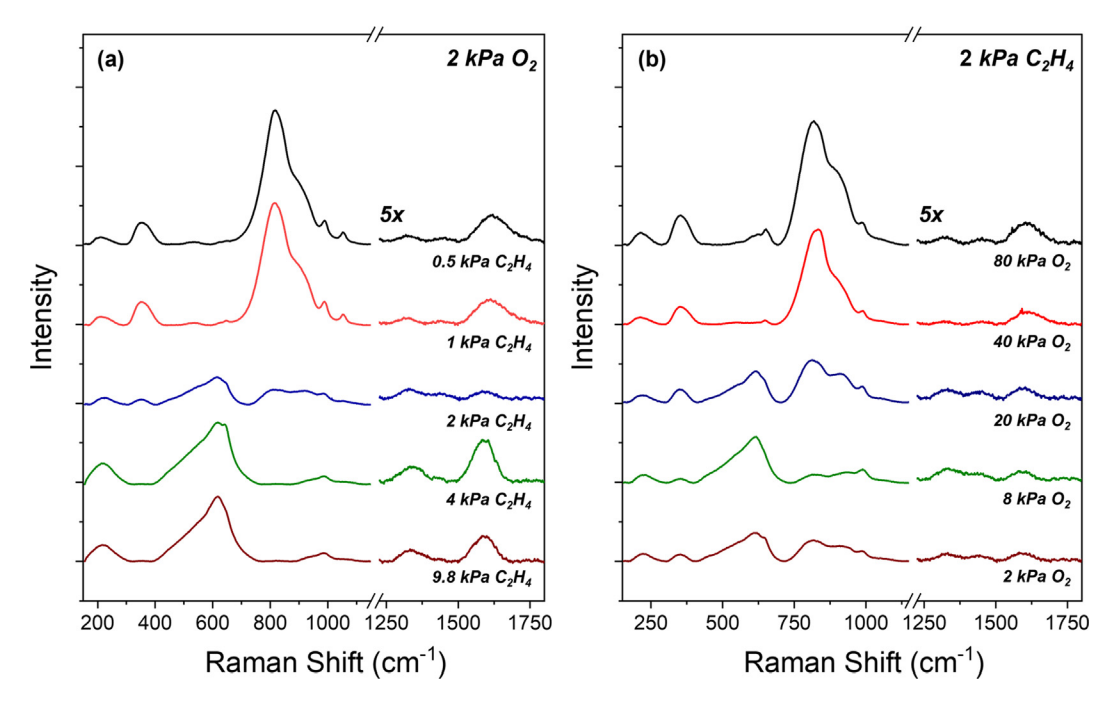


Fig. 2. Steady-state Raman spectra of surface and subsurface species formed on Ag nanoparticles following contact with reactant mixtures for ethylene epoxidation at 523 K with (a) fixed  $O_2$  pressure (2 kPa  $O_2$ ) and increasing  $O_2$  pressure (0.5 – 9.8 kPa  $O_2$ ), and (b) fixed  $O_2$  pressure (2 kPa  $O_2$ ) and increasing  $O_2$  pressure (2 – 80 kPa  $O_2$ ). Spectra were acquired after 2 h contact at indicated conditions. Features above 1200 cm<sup>-1</sup> are multiplied by a factor of five for greater clarity. Spectra acquired for 30 s at 532 nm with low power densities (0.26 mW  $\mu$ m<sup>-2</sup>) following an oxidative treatment (101 kPa  $O_2$ , 673 K, 4 h).

bonates (CO<sub>3</sub>\*), acetaldehyde (CH<sub>3</sub>CHO\*), and associated intermediates. This area of literature contains numerous studies, therefore, discussion here describes only those peaks detected here (Fig. 2). The spectra obtained with  $[C_2H_4]$  to  $[O_2]$  ratios equal to or greater than unity possess features derived from organic surface intermediates that include the pair of features at 1340 and 1590 cm<sup>-1</sup> that have been attributed to CO<sub>3</sub>\* intermediates but are also consistent with C<sub>2</sub>H<sub>4</sub>\* bound to cationic Ag atoms [70,73]. Notable vibrational modes for C<sub>2</sub>H<sub>4</sub>O\* include deformations  $(790 - 890 \text{ cm}^{-1})$  and stretching  $(1250 - 1270 \text{ cm}^{-1})$  of the oxirane ring, the frequencies of which depend upon symmetry and the presence of coadsorbed O\*-atoms [39,42,70,99]. In addition, C<sub>2</sub>H<sub>4</sub>O\* possesses vibrational modes associated with the methylene groups (-CH<sub>2</sub>) at  $\sim$  800 and 1140 cm<sup>-1</sup> [19,41,55,99,100,111]. Chemisorbed acetaldehyde (CH<sub>3</sub>CHO\*) also appears in past work, however, the v(C=0) of this intermediate generally falls between 1680 and 1740 cm<sup>-1</sup> [99], which does not appear in spectra obtained here (Fig. 2). Consequently, we conclude that the organic components present during reactions of C<sub>2</sub>H<sub>4</sub> and O<sub>2</sub> on these Ag nanoparticles most likely include some combination of C<sub>2</sub>H<sub>4</sub>O\* and CO<sub>3</sub>\*, which exist along with varying coverages of reactive oxygen.

Accurate assignment of Raman features and interpretation of their significance is facilitated by MCR–ALS analysis [112,113], which deconvolutes the overlapping features (e.g., in the range of  $600 - 1000 \text{ cm}^{-1}$ ) and explicates how the appearance and loss of these features correlate with each other together with  $[O_2]$  and  $[C_2H_4]$ . Fig. 3 shows the five linearly independent components obtained from analysis of steady-state spectra measured as functions of reactant pressures, which includes those presented in Fig. 2 but also combinations of  $[O_2]$  and  $[C_2H_4]$  between 2 and  $[O_2]$  and

Component one increases with the  $[O_2]$  to  $[C_2H_4]$  ratio (Fig. 2) and contains the broad asymmetric peak at  $\sim 810~\text{cm}^{-1}$  with a shoulder extending to 910 cm<sup>-1</sup> as well as peaks at 350, 990, and 1050 cm<sup>-1</sup>. We assign component one to structures that possess high coverages of monatomic and (or) diatomic surface oxygen based on its dependence on [O<sub>2</sub>] and previous assignments (Table 1). Components two and three both contain a broad feature with a peak that lies between 600 and 620 cm<sup>-1</sup> along with less intense features for component two at 220, 350, and 980 cm<sup>-1</sup> and for component three a peak at 220 and 980 cm<sup>-1</sup>. While the assignment of the 980 cm<sup>-1</sup> peak remains contentious, we tentatively assign features between 220 and 640 cm<sup>-1</sup> to surface and subsurface atomic oxygen [77,78]. While components one, two and three contain many similar features related to reactive oxygen species, the dependence of these features on  $[O_2]$  and  $[C_2H_4]$  differ (hence their appearance as linearly independent contributions to experimental Raman spectra). As ratios of [O<sub>2</sub>] to [C<sub>2</sub>H<sub>4</sub>] increase, components two and three appear initially and component one dominates at the most oxidizing conditions. These trends demonstrate that the species responsible for the  $\sim 810~\text{cm}^{-1}$  band populate only after the Ag surface and near surface region form structures that possess large quantities of atomic oxygen. Thus, the formation of the  $\sim 810~\text{cm}^{-1}$  species becomes exergonic only in the presence of high coverages of other oxygen intermediates.

Component four contains unique features at 785, 910, and 980 cm $^{-1}$  and weaker contributions at 220 and 350 cm $^{-1}$  that appear in components 1 – 3, peaks at 1080 and 1190 cm $^{-1}$ , and broad low intensity features at 1320 and 1590 cm $^{-1}$ , which appear also in other components. The correlated appearance of the 785, 910 and 1080 cm $^{-1}$  peaks suggest the presence of  $C_2H_4O^*$  [70,99] or an oxametallacycle that precede the formation of  $C_2H_4O^*$  [41]. These epoxide-related features become most significant within experimental spectra with the highest  $[C_2H_4]$  to  $[O_2]$  ratios (e.g., ratios of 2 or more) and appear always with significant coverages of structures that contain atomic oxygen (220 and 350 cm $^{-1}$ ). Component five consists primarily of features at  $\sim$  670, 880, 1340 and

**Table 1**Raman Peak Assignments from Previous Literature.

Raman frequencies in	Reported frequencies in	Previously assigned
this work (cm <sup>-1</sup> )	literature (cm <sup>-1</sup> )	vibrational modes
220	240	v(Ag-O <sub>2</sub> )[103]
220	270	v(Ag-O)[104]
	217	$v(Ag-O_2)[104]$ $v(Ag-O_2)[105]$
	210	$v(Ag-O_2)[105]$ $v(Ag-O_2)[106]$
	225	
		$v(Ag-O_2)[73]$
350	270	$v(Ag-OCO_2)[73]$
350	325	v(Ag-O)[103]
	351	$v(Ag-O_{surface})[71,106]$
	335	v(Ag-O)[107]
	350	$\delta(Ag-O_{surface})[73]$
600 – 640	622	$v(Ag-O_2)[71,106]$
	640	$v(Ag-O_{subsurface})$
		[73,78,108]
	630	$v(Ag-O_{subsurface})[77]$
	676	$v(Ag-O_2^{2-})[69]$
	632	$v(Ag-O_{bulk})[76]$
	640	$v(Ag-O_2)[103]$
	697	$v(Ag-O_2^{2-})[107]$
	645	$v(Ag-O_2)[104]$
	650	ν(Ag-O)[105]
	624	$v(Ag-O_2^{2-})[75]$
810 - 820	802	$v(Ag-O_{subsurface})$ [76]
010 020	800	$v(Ag-O_{surface})[59,78]$
	803	$v(Ag-O_{surface})[77]$
	810	$v(Ag-O_{surface})[73]$
	790	$v(Ag-O_{surface})[108]$
	805	$v(Ag-O_2)[74,104]$
	780	
	808	$v(Ag = O_{surface})[108]$
		ν(Ag-O) [75]
200 000	808	v(Ag-O <sub>2</sub> )[109]
890 – 990	890	$v(C_2H_4O^*)[70,99]$
	983	$v(Ag-O_2)[71,106]$
	954	$v(Ag-O_{surface})[76]$
	956	$v(Ag = O_{surface})$ [59]
	995	$v(Ag-O_2^-)[69]$
	960	$v(Ag-O_2^-)[108]$
	951	v(Ag-O)[105]
	950	$v(Ag-O_{surface})[77]$
1050	1072	$v(CO_3^{2-})[70]$
	1053	$v(Ag-O_2^-)[107]$
	1078	$v(Ag-O_2^{2-})[75]$
	1054	$v_{\rm s}({\rm CO_3})[73]$
1200	1245	$v(C_2H_4O^*)[70]$
1340	1320	$v(Ag-O_2)[104]$
	1332	$\delta(C_2H_4^*)[109]$
	1333	$v_{as}(CO_3)[73]$
	1310 - 1320	$v(C_2H_4^*)[110]$
	1365	$v(CO_3^{2-})[70]$
1590	1570 - 1579	$v(C_2H_4^*)[110]$
1550	1596	$v(C_2^{114})[110]$ $v(CO_3^{2-})[70]$
	1330	F(CO3 )[70]

1590 cm<sup>-1</sup> and exists at low coverages across the full range of conditions examined, however, component five reaches the greatest contribution to spectra at high ratios of [O<sub>2</sub>] to [C<sub>2</sub>H<sub>4</sub>]. The combination of peaks indicates that component five represents a combination of monodentate and bidentate carbonate species (CO<sub>3</sub>\*) that form during the complete combustion of C<sub>2</sub>H<sub>4</sub> [70,114]. Taken together, components four and five suggest that C<sub>2</sub>H<sub>4</sub>O\*, CO<sub>3</sub>\* and potentially C2-oxametallacycles comprise the majority of organic surface intermediates present at these conditions. The relative coverage of C<sub>2</sub>H<sub>4</sub>O\* to CO<sub>3</sub>\* decreases systematically with the ratio of [C<sub>2</sub>H<sub>4</sub>] to [O<sub>2</sub>], which appears consistent with the expectation that these species compete for binding sites and lie at different points along the reaction coordinate for ethylene oxidation. Undoubtedly, other organic species coexist but likely at low coverages that provide smaller contributions to experimental spectra. Extinction coefficients for these intermediates and their vibrational

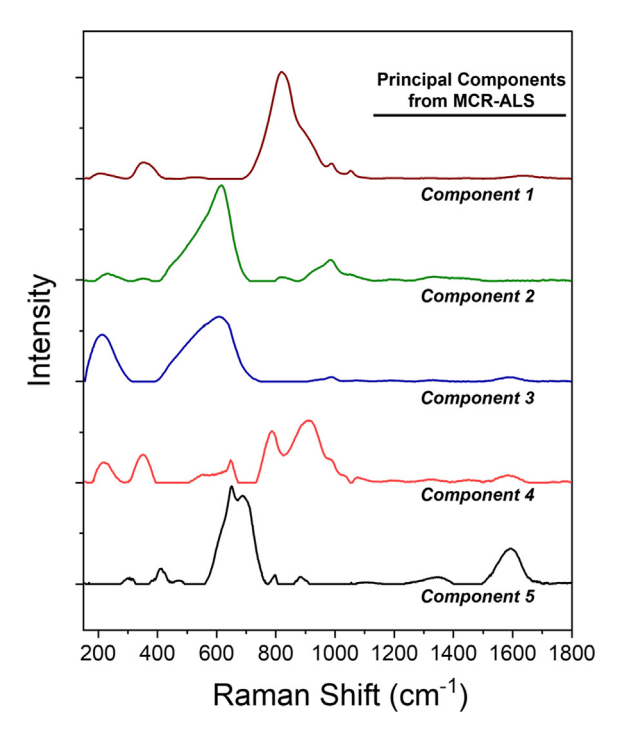


**Fig. 3.** Principal components derived from Raman spectra (Fig. 2) of intermediates formed by contact of  $C_2H_4$  and  $O_2$  reactants with Ag nanoparticles at 523 K. Plausible assignments include (1) surface atomic and diatomic oxygen surface species, (2) subsurface atomic oxygen, (3) bulk oxygen, (4)  $C_2H_4O^*$ , and (5)  $CO_3^*$ . Spectra were acquired at 532 nm with low power densities (0.26 mW  $\mu$ m $^{-2}$ ) following an oxidative treatment (101 kPa  $O_2$ , 673 K, 4 h).

modes are unknown, therefore, absolute coverages cannot be compared.

Overall, in situ Raman spectra obtained during reactions of C<sub>2</sub>H<sub>4</sub> and O<sub>2</sub> on Ag nanoparticles (Fig. 2 and Fig. 3) show that a broad distribution of reactive oxygen species coexist upon the surface with organic species formed by oxidation of C<sub>2</sub>H<sub>4</sub>. The numbers and distributions of the oxygen species depend strongly upon the reactant pressures, which implies that distributions of oxygen obtained at much lower pressures and in the absence of C2H4 on Ag nanoparticles or low-index Ag surfaces and ab initio calculations of these structures [15,34,39,41,50,115] will differ significantly from those obtained at the reactant pressures implemented for ethylene epoxidation on supported catalysts Ag [19,21,70,98,116,117]. These distinctions likely extend beyond differences in reactant coverages and could include catalytically significant variations in the bulk phase of the Ag-based catalyst, the amount of subsurface oxygen, and the appearance of surface reconstructions (even in the absence of chlorine and other promoters). The importance of these possibilities appear in discussions in foundational papers for this reaction [15,32,34,35,39,41,50,97,115,118 ,119]. While peak assignments for many of the O<sub>2</sub>-derived features remain somewhat uncertain, the intermediate responsible for the  $\sim 810 \text{ cm}^{-1}$  band that dominates Raman spectra at high  $[O_2]$  to [C<sub>2</sub>H<sub>4</sub>] ratios and its significance for ethylene epoxidation remains debated with claims for both atomic and diatomic oxygen intermediates. We find that this complex only appears in the presence of high amounts of surface and subsurface atomic oxygen and disappears with increasing [C<sub>2</sub>H<sub>4</sub>]. The prominence of this feature and its plausible involvement in ethylene epoxidation motivate further experiments and computations to determine the structure of the corresponding species and the site requirements to stabilize this intermediate.

## 3.3. In situ Raman during oxidative treatments of Ag and Ag<sub>2</sub>O nanoparticles

To determine the dependence of the reactive oxygen surface species on the underlying composition and structure of Ag nanoparticles, we collected Raman spectra in the absence of ethylene from Ag and Ag<sub>2</sub>O nanoparticles. Fig. 4 shows spectra acquired by exposing pelletized Ag or Ag<sub>2</sub>O nanoparticles to flowing O<sub>2</sub> (101 kPa O<sub>2</sub>) and heating incrementally from 523 to 673 K in 50 K increments before returning to 523 K. The temperature was held constant for 3 h at each set of conditions, and spectra did not show measurable changes after 1.5 h at each temperature. While spectra in Fig. 4 appear to represent steady-state at these timescales, comparisons among spectra obtained either from Ag or Ag<sub>2</sub>O nanooparticles at 523 K at the beginning and end of each sequence demonstrate these signify kinetically trapped states and not equilibrated structures. These spectra show Ag and Ag<sub>2</sub>O nanoparticles share similar peaks, but with different intensities.

In comparison, Fig. 4b shows Raman spectra obtained from the Ag<sub>2</sub>O nanoparticles throughout the course of an identical oxidative treatment, and these spectra remain largely constant. The initial spectrum obtained possesses an intense scattering feature at  $\sim 990~{\rm cm}^{-1}$  and much weaker peaks at 240, 350, 620,  $\sim 830$ , and  $1080 \text{ cm}^{-1}$  (101 kPa  $O_2$ , 523 K). These peaks undergo minimal changes following higher temperature annealing in O2. During this process, the most notable difference is an increase in the intensity of the 830 cm<sup>-1</sup> peak relative to other features (e.g., 990 cm<sup>-1</sup>). Following treatment at 673 K and cooling to 523 K, the intensity of the 830 cm<sup>-1</sup> peak increases substantially in comparison to other features, and a new shoulder emerges near 900 cm<sup>-1</sup>. Diffraction patterns before and after these treatments (Fig. 1) contain only peaks representative of crystalline Ag<sub>2</sub>O, which seems consistent with the small differences between Raman spectra before and after oxidation

These comparisons provide insight to the significance of the changes in the Ag nanoparticles during oxidation but also raise further questions. First, the appearance of Raman features between 200 and 500 cm<sup>-1</sup> represent high coverage of atomic oxygen both at and beneath the surface of Ag nanoparticles (Fig. 4a), however, these features do not match the intensity or line shape of the comparable range of the spectra obtained from Ag<sub>2</sub>O nanoparticles (Fig. 4b). This, together with XRD patterns that correspond only to metallic Ag, indicate that the surface and near-surface region ( $\sim$ 2 nm) of the Ag nanoparticles contain significant amounts of oxygen but the bulk of the nanoparticles remain reduced following these treatments (101 kPa O<sub>2</sub>, 523 - 673 K, cumulative 15 h). Second, the spectra of Ag<sub>2</sub>O appear similar before and after oxidative treatments (Fig. 4b), especially below  $\sim 650~\text{cm}^{-1}$  where prior investigations consistently assign Raman peaks to structures that involve atomic oxygen including those within the bulk of the nanoparticle [59,73,76-78,120]. Third, the small changes that do appear only involve oxygen species with features at frequencies>800 cm<sup>-</sup> [121]. Intuitively, these thermal treatments cannot increase the oxidation state or bulk oxygen content of Ag<sub>2</sub>O, therefore, the appearance of these features reflect the evolution of the surface structure or composition. Fourth, the Raman spectra and XRD patterns of Ag and Ag<sub>2</sub>O nanoparticles differ following this extended series of oxidative treatments, which demonstrates the surface reactions and subsurface diffusion processes responsible for adding or removing oxygen from these materials do not reach equilibrium but are kinetically limited. Temperature programmed experiments indicate that Ag<sub>2</sub>O nanoparticles autoreduce near 700 K in inert environments [105,122,123], which together with computed phase diagrams (vide infra) suggest that the persistent oxygen-derived surface layers reflect large kinetic barriers for recombinative desorption of  $O_2$ . Despite these observations, the precise peak

assignments for most features in these spectra remain uncertain, and the contradictory assignments from literature cannot be reconciled. Accordingly, the nature of the elementary processes that form these structures and their functional dependence upon one another are unknown. These points may be addressed, however, by using *ab initio* calculations to determine the vibrational frequencies of plausible surface structures that contain Ag and oxygen, and comparison to spectrokinetic measurements of the oxidation and reduction of these structures (*vide infra*).

## 3.4. Computed free energies and vibrational frequencies of Ag<sub>x</sub>O<sub>y</sub> surfaces

To address ambiguities regarding assignments for vibrational frequencies on oxygen-containing Ag surfaces, we examined proposed molecular models for variable stoichiometry  $Ag_xO_y$  surfaces (Fig. 5). Before computing vibrational frequencies, we first evaluated the relative stability of different  $Ag_xO_y$  surfaces to screen for candidate structures that may form exergonically during exposure of Ag nanoparticles to either  $O_2$  alone (Fig. 4) or in mixtures of  $C_2H_4$  and excess  $O_2$  (Fig. 2). We optimized structures (Section 2.4) of oxygen-containing reconstructed and unreconstructed Ag (111) and Ag (100) terraces, and Ag (110) and Ag (311) steps as models for the 80-100 nm Ag nanoparticles used here (Section 2.1 and Section 3.1). Fig. 5 reports the 49  $Ag_xO_y$  surfaces computed here; individual references for the source of each structure are tabulated in Table S2.

To identify low free energy surfaces at the experimental conditions (2 - 101 kPa O<sub>2</sub> and temperatures from 523 to 673 K, corresponding to an oxygen chemical potential,  $\Delta\mu_0$ , range of -72 to  $-50 \text{ kJ} \text{ mol}^{-1}$ ) we computed the Gibbs free energy (per area) for each surface using eq. (1) (Section 2.4.2). Fig. 6 and Fig. 7 show the lowest free energy structures for each facet as a function of temperature and [O2]. Surface phase diagrams as a function of  $\Delta\mu_0$  for all computed structures [60,124-128] are reported in Section S.4. To estimate where the metal to metal-oxide phase transition occurs we chose Ag<sub>2</sub>O as the bulk oxide reference [129]. Bulk Ag<sub>2</sub>O formation is not favorable at the experimental conditions used here [130,131]. Therefore, when the initial state of the catalyst is a Ag nanoparticle we expect Ag<sub>x</sub>O<sub>v</sub> surfaces to be predominant in O2 alone (Fig. 4a) or in large stoichiometric excesses of O<sub>2</sub> in mixtures that contain C<sub>2</sub>H<sub>4</sub> (Fig. 2, black and red lines, and Fig. 3, principle component 1). The similarities between Raman spectra under these conditions suggests that the presence of C<sub>2</sub>H<sub>4</sub> does not strongly impact the forms of reactive oxygen present on surfaces, and we have consequently omitted adsorbed C<sub>2</sub>H<sub>4</sub> from the subsequent calculations.

Fig. 6a reports the relative stability of Ag (111) surfaces; the  $Ag_{1,2}O_{asym}$  and Ag(111) are the most stable structures in the range of temperatures (523 - 673 K) and oxygen partial pressures (2 -101 kPa O<sub>2</sub>) examined here (Fig. 2 and Fig. 4). There are several reported phase diagrams for Ag (111) [58,119,127,132,133], however, these do not contain all of the structures computed here. The  $c(4 \times 8)$  surface is the most stable at  $\Delta\mu_0$  from -40 to -30 kJ mol<sup>-1</sup>, consistent with Martin et al. [58], and the Ag<sub>1.2</sub>O<sub>asym</sub> is the most stable phase from -60 to -40 kJ mol<sup>-1</sup>, consistent with calculations from Michaelides et al. [127]. We also evaluated the free energies of proposed Ag<sub>10</sub>O<sub>7</sub> and Ag<sub>3</sub>O<sub>4</sub> surfaces from a recent Grand Canonical Monte Carlo (GCMC) study (Section S.4), however, these structures are higher in energy than those reported in Fig. 6a. The  $p(7 \times 7)_{1\text{layer}}$ , Ag<sub>1.33</sub>O, Ag<sub>16</sub>O, Ag<sub>1.83</sub>O, and  $p(4 \times 4)$  surfaces are not the lowest free energy surfaces and hence do not appear in Fig. 6a. However, since these structures form exergonically at different points in the range of experimental conditions of interest (Section

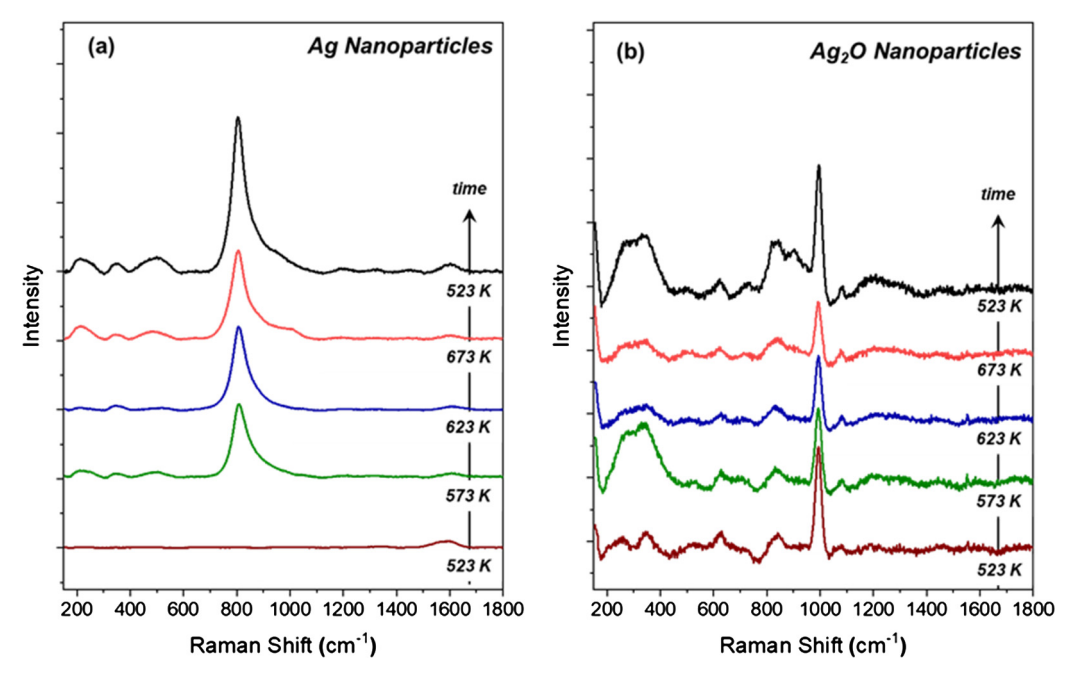


Fig. 4. Steady-state Raman spectra obtained from (a) initially reduced Ag nanoparticles, and (b)  $Ag_2O$  nanoparticles. Materials were heated from ambient temperature to incrementally greater temperatures as indicated within flowing oxygen (101 kPa  $O_2$ ). Spectra were acquired continuously for 3 h at 532 nm with low power densities (0.26 mW  $\mu$ m<sup>-2</sup>), and samples were not oxidatively treated beforehand.

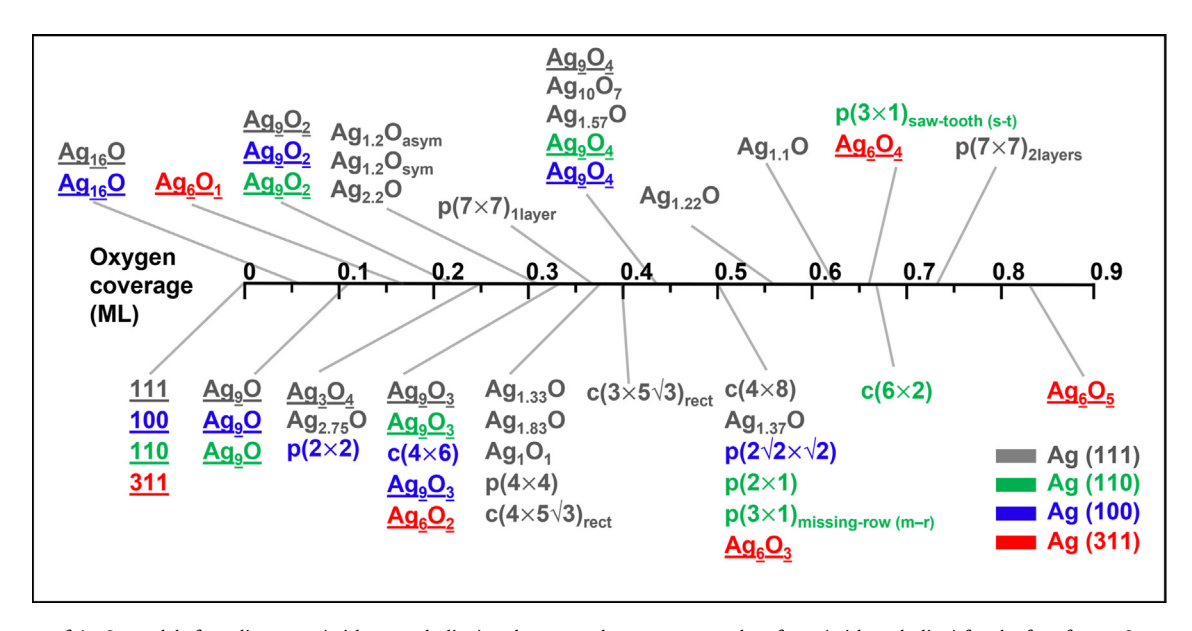


Fig. 5. Summary of  $Ag_xO_y$  models from literature (without underline) and generated unreconstructed surfaces (with underline) for the four facets. Oxygen coverages for terraces, (111) and (100), are defined as the number of surface oxygen atoms divided by the number of Ag atoms in each unreconstructed layer, according to [58]. For steps, (110) and (311), the coverage is defined as the number of surface oxygen atoms divided by the number of surface Ag atoms as in [119].

S.4), we considered them in our analysis of vibrational frequencies (vide infra), in addition to the  $Ag_{1.2}O_{asym}$ , and  $c(4 \times 8)$  surfaces.

The Ag (110) surface has multiple reconstructions reported under oxidizing conditions [50,134,135]. Fig. 6b shows that as  $\Delta\mu_0$  increases, the most stable phase transitions from  $p(3\times1)_{\rm m-r}$ , to  $p(2\times1)$ , and finally to  $c(6\times2)$ . The evolution of these species agrees with the *ab initio* (110)–(T, p) phase diagram from Jones et al. [119]. These predictions are also consistent with experimental LEED patterns of  $p(2\times1)$  acquired by Campbell et al. under UHV conditions [51]. The  $p(3\times1)_{\rm s-t}$  reconstruction possesses a free energy similar to the  $p(3\times1)_{\rm m-r}$ ,  $p(2\times1)$ , and  $c(6\times2)$  surfaces,

therefore we also considered this surface in subsequent calculations.

Few reports discuss reconstruction of the Ag (100) or Ag (311) surfaces. With increasing  $\Delta\mu_0$  the most stable surfaces for Ag (100) were 0.11 ML, 0.22 ML, 0.33 ML, and (100)– $p(2\sqrt{2}\times\sqrt{2})$ –0 (Fig. 7a). The  $p(2\sqrt{2}\times\sqrt{2})$  reconstruction is the most stable surface between  $\Delta\mu_0$  ranging from -55 to -40 kJ mol $^{-1}$  (Section S.4), consistent with calculations from Costina et al. [136]. However, the  $c(4\times6)$  and  $p(2\times2)$  surfaces they report are higher in energy than the unreconstructed 0.22 ML and 0.33 ML structures we generated on Ag (100). Fig. 7b reports the lowest free energy structures for

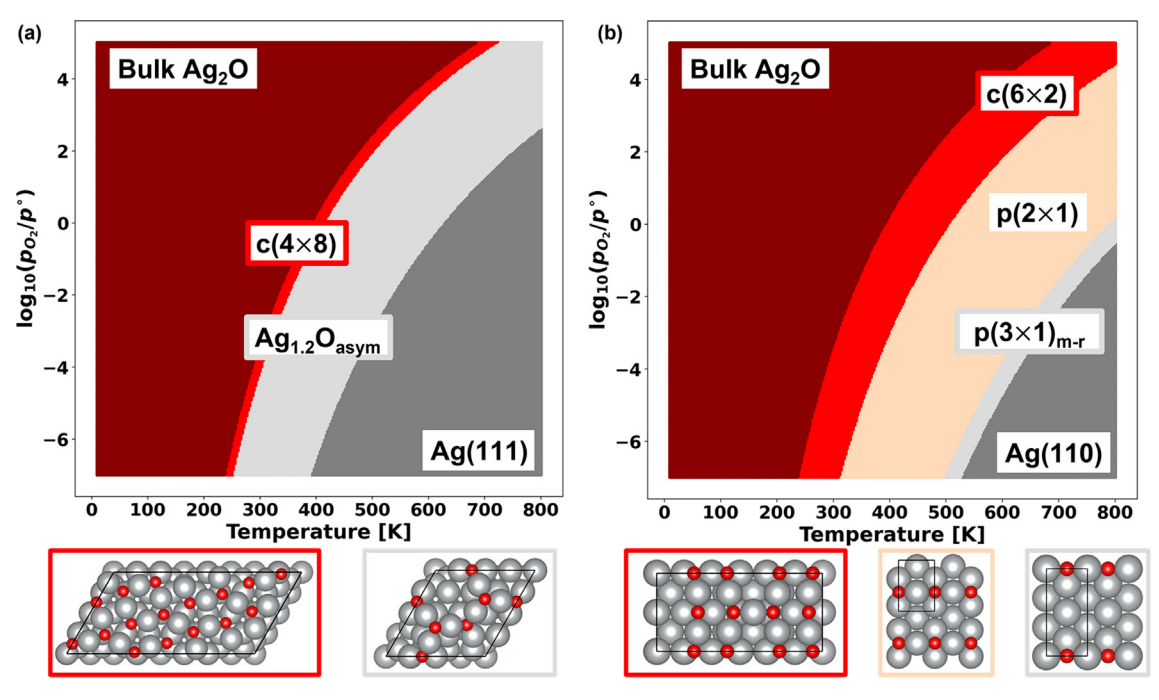


Fig. 6. Ab initio phase diagrams for the (a) Ag (111)–O surfaces and (b) Ag (110)–O surfaces. Corresponding minimum free energy structures are shown below each phase diagram. Black lines denote the unit cells. The O atoms are red and Ag atoms are silver.

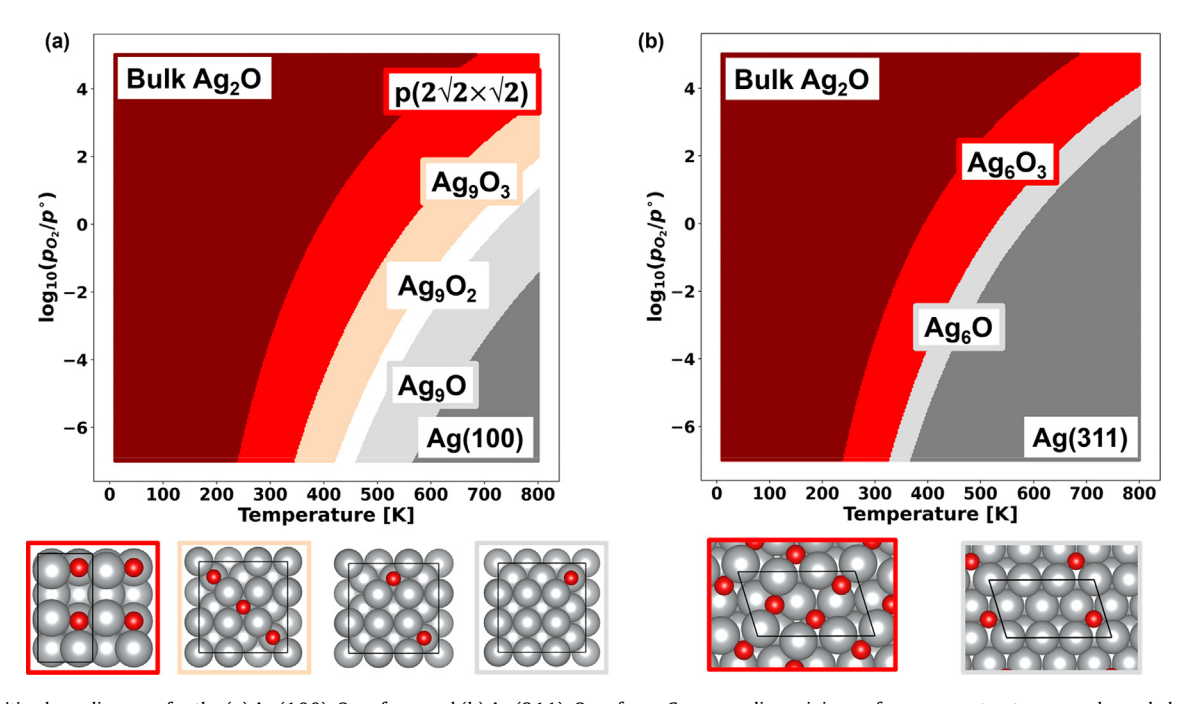


Fig. 7. Ab initio phase diagrams for the (a) Ag (100)–O surfaces and (b) Ag (311)–O surfaces. Corresponding minimum free energy structures are shown below each phase diagram. Black lines denote the unit cells. The O atoms are red and Ag atoms are silver.

Ag (311), which are the unreconstructed 0.5 ML and 0.17 ML surfaces. As far as we are aware, phase diagrams for oxygen adsorption and reconstruction of Ag (311) are not available for comparison. Summarizing, out of the 49 initial candidate structures on the four Ag facets, 22 structures are computed to form exergonically within the range of experimental conditions used here (523 – 673 K, and 2 – 101 kPa  $\rm O_2$ ).

We next computed vibrational frequencies for all minimum free energy structures reported in the phase diagrams (Fig. 6 and Fig. 7), and higher free energy structures that do not appear on the phase diagrams but form exergonically under the experimental conditions of interest (Section S5). Table 2 summarizes the maximum frequency computed for each structure on the phase diagrams, and the complete set of vibrational frequencies for all structures that form exergonically at 523 - 673 K and 2 - 101 kPa  $O_2$  are shown in **Figure S5** and **Figure S6** and tabulated in Table S3. The computed frequencies for all surfaces were below  $602 \text{ cm}^{-1}$ . Computed frequencies can generally be assigned to three different vibrational modes: v(Ag-O) modes of atomic oxygen ( $205 - 399 \text{ cm}^{-1}$ ), symmetric O-Ag-O stretches ( $360 - 531 \text{ cm}^{-1}$ ), and

**Table 2**Maximum Calculated Frequencies for All Minimum Free Energy (111), (110), (100), and (311) Surfaces.

Structure	Facet	Maximum Calculated Frequency (cm <sup>-1</sup> )
$p(2 \times 1)$	110	601
$p(3 \times 1)$	110	584
$p(2\sqrt{2}\times\sqrt{2})$	100	562
$p(6 \times 2)$	110	555
$Ag_6O_3$	311	515
$c(4 \times 8)$	111	512
$Ag_{1.2}O_{asym}$	111	500
$Ag_9O_2$	100	477
$Ag_9O_3$	100	422
Ag <sub>6</sub> O	311	312
$Ag_9O_1$	100	304

asymmetric O–Ag–O stretches (417 – 601 cm<sup>-1</sup>). Our results encompass a similar range of vibrational frequencies to those reported by Li et al. (200 – 526 cm<sup>-1</sup>) [137] and Gajdoš et al. (238 – 400 cm<sup>-1</sup>) [138] for surface and subsurface O–containing Ag (111), and Ag (100) structures, respectively. Frequencies > 492 cm<sup>-1</sup> appear only on reconstructed surfaces and 0.5 ML coverage Ag (311) steps (**Figure S5** and **Fig.** 7b) and arise only from O–Ag–O vibrations. The O–Ag–O motif can be composed of either surface or subsurface O, where we define surface O-atoms as those whose nuclei lie above that for the outermost layer of Ag atoms, and subsurface O as those atoms with nuclei that reside below those of the first layer of Ag atoms. The v(Ag–O) modes at 205 – 399 cm<sup>-1</sup> correspond to surface and subsurface atomic oxygen on both reconstructed and unreconstructed surfaces, consistent with previous literature assignments [71,104–107].

Frequency calculations enable us to make several assignments for the experimental spectra in Fig. 2, Fig. 3 and Fig. 4. Computed frequencies are consistent with the assignment of the 350 cm<sup>-1</sup> band that appears in both pure O2 (Fig. 4a) and cofed ethylene (Fig. 2) to v(Ag-O) modes of surface atomic oxygen [71,106]. We assign the broad band centered between 600 and 620 cm<sup>-1</sup> (Fig. 2. Fig. 3 principal components 2 and 3) to asymmetric O-Ag-O vibrations. These O-Ag-O motifs form only on reconstructed surfaces or Ag (311) steps at 0.5 ML coverage, and can contain either surface (e.g.  $110-p(2 \times 1)$ ) or subsurface atomic oxygen (e.g. 111-Ag<sub>1,2</sub>O<sub>asym</sub>). The O-Ag-O motifs are similar to O-Au-O complexes formed on Au nanoparticles that are reported to have vibrational frequencies in the range of 500-600 cm<sup>-1</sup> [121]. The O-Ag-O motif does not form on unreconstructed (111), (110), or (100) surfaces, thus vibrational frequencies corresponding to its appearance are a molecular fingerprint for surface oxidation and reconstruction. The Raman features attributed to asymmetric O-Ag-O vibrations (near 600 cm<sup>-1</sup>) decrease as surfaces become more oxidized, which is evident for Ag<sub>2</sub>O nanoparticles (Fig. 4b) and for Ag nanoparticles (Fig. 2 black and red lines, and Fig. 4a) exposed to increasing O<sub>2</sub> to C<sub>2</sub>H<sub>4</sub> ratios. These changes do not reflect the loss of the surface reconstruction or the O-Ag-O motifs, rather, the attenuation of the Raman peak originates from a decrease in the Raman scattering intensity of these vibrational modes as the oxygen content increases [77]. These earlier interpretations are consistent with differences in the computed Raman intensities of asymmetric O-Ag-O vibrations in bulk Ag<sub>2</sub>O (SI Section S7).

None of our computed structures (**Figures S5 and S6**) explain the broad and prominent features near 810 cm<sup>-1</sup> [75,76] derived from oxygen during ethylene epoxidation (Fig. 2) or during oxidative treatments (Fig. 4a). Vibrational frequencies > 800 cm<sup>-1</sup> are uncharacteristic for forms of atomic oxygen either at low coverages on metallic transition metal surfaces [139,140], within high coverage adlayers, or for reconstructed surface oxides [80,97,119]. The molecular models discussed above, and widely used in the litera-

ture, only contain surface and subsurface atomic oxygen, and do not explicitly consider the diatomic oxygen species proposed in earlier vibrational spectroscopy studies of  $O_2$  adsorption to metal surfaces that reported features near  $800-1000~\rm{cm}^{-1}$  [69,74,141,142].

To explore this possibility, we generated dioxygen species on Ag surfaces using the reconstructed and unreconstructed Ag surfaces that appear on our phase diagrams (Fig. 6, Fig. 7, Table 2). Dioxygen containing surfaces were generated at both equal and higher oxygen coverages (additional details in Section S.5.2) than the originating phase diagram structure, and reaction free energies for dioxygen formation were computed using eq. (4):

$$\Delta G(T, p_{O_2}) = E_{\text{ref} + xO} - E_{\text{ref}} - x\mu_0(T, p_{O_2})$$
 (4)

where  $\Delta G$  is the Gibbs free energy of reaction,  $E_{\rm ref}$  is the computed energy of the respective phase diagram structure,  $E_{\rm ref+x0}$  is the energy of the corresponding dioxygen containing structure, and x is the number of additional oxygen atoms included to generate the dioxygen containing structures. Table 3 shows that regardless of surface and coverage, all dioxygen species form endergonically (+70 to +225 kJ mol<sup>-1</sup>) at 523 K, 101 kPa  $O_2$ . Based on the evidence presented above, we conclude that the  $\sim$  810 cm<sup>-1</sup> peak present at 523 K does not arise from atomic surface or subsurface O, or adsorbed diatomic oxygen species on the metallic or reconstructed surfaces proposed in the literature.

Having excluded the reconstructed and unreconstructed surfaces proposed in the literature, and the formation of diatomic oxygen on these surfaces, we next considered the possibility that in the presence of oxygen (Fig. 4a), or ethylene and oxygen in stoichiometric excess (Fig. 2), the Ag surface may resemble a thin oxide film, as proposed by Ozbek et al. [32,118] and Fellah et al. [45]. Experimentally, STM images from Derouin et al. [62] showed development of a bulk-like Ag<sub>2</sub>O thin film with atomic oxygen dosing on Ag (111) surface at 500 K. Further, DFT calculations from Xu et al. show that the binding energy of oxygen on Ag becomes more exothermic as the number of subsurface oxygen increases [63]. Moreover, similar Raman peak locations are observed for both Ag and Ag<sub>2</sub>O nanoparticles exposed to 101 kPa O<sub>2</sub> (Fig. 4), suggesting some similarity between the surface structure of these two materials. Based on these evidence, we next explored the possibility that an Ag<sub>2</sub>O-like surface, which is thicker than the widely discussed Ag<sub>2</sub>O tri-layer surfaces considered in our phase diagram calculations (e.g.  $Ag_{1.2}O_{asym}$ ) [63,119,133,137,143,144], may form under oxidizing conditions.

## 3.5. Gibbs free energies and frequencies for dioxygen species on an oxide slab model

We explored formation of diatomic oxygen species on the widely used  $Ag_2O(001)$  oxide slab model [32,33,35-37,45] starting from different exposed lattice oxygen coverages. We systematically examined symmetrically unique combinations of three possibilities (O vacancy, atomic O, and  $O_2$ ) for each of the four surface sites (Fig. 8a) of the  $(2 \times 2)$   $Ag_2O(001)$  slab with five layers. We generated multiple initial guesses for each structure and then optimized the structures. Reaction free energies were calculated at 523 K and 101 kPa  $O_2$  according to:

$$\Delta G \Big( T, p_{\rm O_2} \Big) = E_{\rm Ag_2O + xO} - E_{\rm Ag_2O} - x \mu_{\rm O}(T, p_{\rm O_2}) \eqno(4)$$

where  $E_{Ag_2O+xO}$  is the energy of the dioxygen and (or) vacancy containing slab,  $E_{Ag_2O}$  is the energy of the Ag<sub>2</sub>O (001) surface, and x is the number of additional oxygen atoms included for generating dioxygen containing structures and ranges from -4 (four vacancies)

**Table 3**Calculated Reaction Energies and Free Energies (523 K, 101 kPa O<sub>2</sub>) for Dioxygen Formation On Phase Diagram Structures.

Facet	Structure	Oxygen Change	Calculated Reaction Free Energy (kJ mol <sup>-1</sup> )	Calculated Reaction Energy (kJ $mol^{-1}$ )
111 $c(4 \times 8)$ Ag <sub>1.2</sub> O <sub>asym</sub>	c(4 × 8)	0	+183	+133
	, ,	+1	+118	+68
	+2	+129	+77	
	$Ag_{1.2}O_{asym}$	0	+225	+175
		+1	+198	+147
		+2	+181	+129
110 $c(6 \times 2)$ $p(2 \times 1)$	$c(6 \times 2)$	0	+180	+130
		+1	+112	+62
		+2	+164	+112
	$p(2 \times 1)$	0	+181	+131
		+1	+130	+80
	+2	+158	+106	
	$p(3 \times 1)$	0	+183	+133
		+1	+138	+87
		+2	+86	+34
100 $p(2\sqrt{2} \times \sqrt{2})$ AgoO	$p(2\sqrt{2}\times\sqrt{2})$	0	+156	+106
		+1	+138	+88
		+2	+163	+111
	$Ag_9O$	+1	+82	+30
		+2	+70	+18
${ m Ag_9O_2}$ ${ m Ag_9O_3}$	$Ag_9O_2$	0	+109	+57
	+1	+94	+42	
		+2	+93	+42
	$Ag_9O_3$	0	+113	+62
		+1	+104	+52
		+2	+130	+78
311	Ag <sub>6</sub> O	+1	+77	+27
		+2	+121	+69
	$Ag_6O_3$	0	+117	+67
		+1	+125	+73
		+2	+159	+107

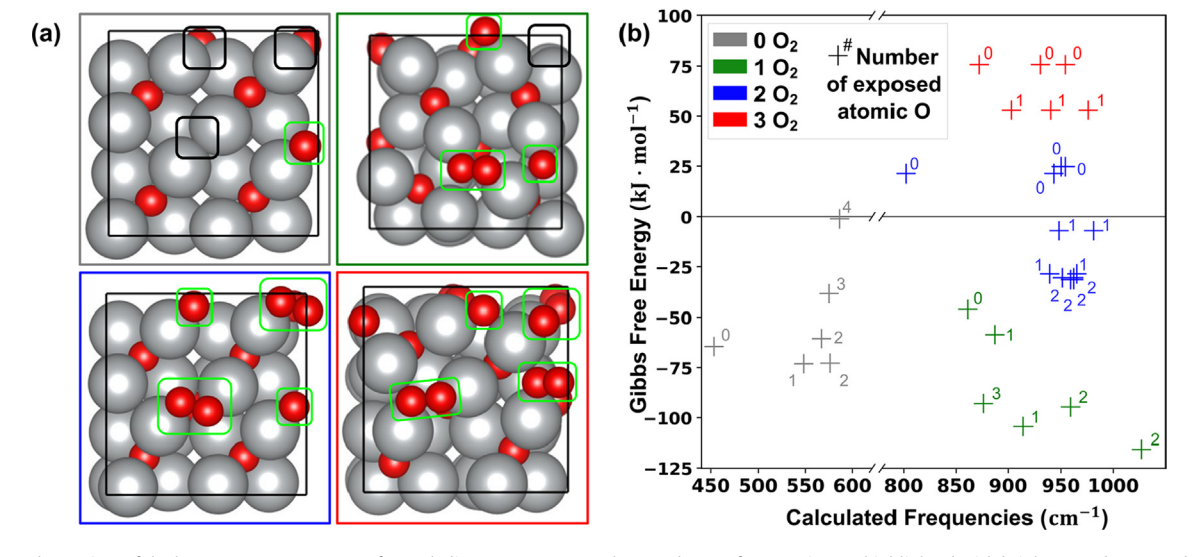


Fig. 8. (a) Top-down view of the lowest energy structures for each dioxygen coverage. The O and  $O_2$  surface species are highlighted with bright green boxes, and vacancies are highlighted with black boxes. (b) Gibbs free energies (523 K, 101 kPa  $O_2$ ) calculated according to eq. (4) and frequencies for varying surface coverages of O vacancies, atomic O and  $O_2$  species on the (2  $\times$  2) Ag<sub>2</sub>O (001) surface. Each structure has four adsorption sites; colors represent the number of dioxygen species and superscripts are the number of exposed atomic O; the remainder of the sites are O vacancies.

to +4 (four dioxygen). For each specific combination of vacancies, atomic oxygen, and diatomic oxygen, we selected the lowest energy structure and computed its vibrational frequencies. Fig. 8b and Table S4 report the relative free energies and maximum computed frequencies for each configuration; the complete set of vibrational frequencies for each structure are shown in Figure S7. For structures with multiple dioxygen, frequencies associated with each dioxygen are shown. Oxygen in the bulk of the Ag<sub>2</sub>O slab have high Raman intensity vibrations at 230 and 390 cm<sup>-1</sup> that correspond to v(Ag-O) and rocking O-Ag-O vibrations, respectively (SI Section

S.7). All oxide slabs (except the four-vacancy structure) have frequencies between 500 and 586 cm<sup>-1</sup> that correspond to asymmetric O-Ag-O stretches that arise from surface and subsurface oxygen. Supporting Information Figure S7 and Table S5 show that computed frequencies and Raman intensities of O-Ag-O vibrations both attenuate with increasing coverage of dioxygen species on Ag<sub>2</sub>O surfaces. Therefore, we expect these modes to possess low Raman scattering intensities when the catalyst surface is oxygen saturated, consistent with earlier interpretations by Ertl and coworkers [77]. Oxide slabs that contained only combinations of atomic O

and vacancies have frequencies that are all below 586 cm<sup>-1</sup>, in agreement with our previous observations for atomic O on low and high coverage surfaces in **Section 3.4**.

In contrast to metallic surfaces, several dioxygen containing structures form exergonically (Fig. 8b) on the Ag<sub>2</sub>O (001) surface. The dioxygen species are located in sites that are occupied by atomic lattice O in the Ag<sub>2</sub>O (001) structure, have frequencies above 800 cm<sup>-1</sup>, and have exergonic free energies at 523 K that indicate they would be expected to persist at high temperatures (>380 K), unlike previously identified molecular oxygen species adsorbed to Ag [17,106,115]. Our results conflict with a previous report of the highly endothermic (+255 kJ mol<sup>-1</sup>) adsorption of O<sub>2</sub> on Ag<sub>2</sub>O (001) oxygen vacancies [32], likely due to unbroken symmetry of the surface in the prior study. Our computed frequencies for these structures range from 802 to 1027 cm<sup>-1</sup>, consistent with the higher frequency band observed when O<sub>2</sub> contacts Ag or Ag<sub>2</sub>O surfaces (Fig. 4) and during ethylene epoxidation in stoichiometric excesses of O<sub>2</sub> (Fig. 2). Effective Bader charge analysis (Section S.8) of these structures shows that dioxygen complexes are more electrophilic (-0.28 |e| to -0.43 |e|) than the atomic oxygen embedded in the surface of or in the bulk of the  $Ag_2O$  slab (-0.89|e| to -1.03 |e|). These dioxygen complexes may correspond to XPS O 1 s features that have higher photoelectron binding energies (>530 eV) than other oxygen species (528 - 529 eV) present on the surface during steady-state reaction with a 1:2 ratio of [C<sub>2</sub>H<sub>4</sub>] to  $[O_2]$  [64,67]. Within Fig. 2a, components one and two, which dominate at the greatest ratios of [O<sub>2</sub>] to [C<sub>2</sub>H<sub>4</sub>], both contain features that align with those consistent with the diatomic species expected upon oxide surfaces. Upon Ag nanoparticles annealed in pure  $O_2$  (Fig. 4a), the asymmetric feature at  $\sim 810 \text{ cm}^{-1}$  and with a broad shoulder extending to nearly 1000 cm<sup>-1</sup> suggests a distribution of dioxygen species that reflects different coordination, orientation, and coverage of dioxygen species across different sites. This interpretation appears consistent also with the Raman spectra of Ag<sub>2</sub>O nanoparticles in contact with O<sub>2</sub> at elevated temperatures (Fig. 4b), which contain clearly distinguishable distributions of states between 800 and 1000 cm<sup>-1</sup> at 523 K following the oxidative treatment and annealing. This thermal treatment likely improves the distinction between these dioxygen species by increasing the order within the surfaces of the Ag<sub>2</sub>O particles (created by precipitation of Ag complexes in basic solutions). The majority of computed dioxygen containing structures reside in the  $850 - 1000 \, \text{cm}^{-1}$  range, which is shifted to higher wavenumber in comparison to Fig. 2 and Fig. 4. The exact oxide film surface structure remains unknown, and as suggested in prior studies [32,33,35-37,45], the Ag<sub>2</sub>O (001) slab is only an approximation of the oxide film that encapsulates the Ag particles (that maintain a metallic core as shown in XRD experiments in Section 3.1). Therefore, we rationalize that the shift in frequencies could be due to the real catalyst surface not being stochiometric and (or) due to the strain created by the lattice mismatch of an oxide film at a metal interface.

Fig. 9 summarizes the computed frequency ranges and assignments based on our analysis of 49  ${\rm Ag_xO_y}$  structures and 21  ${\rm Ag_2O}$  surfaces. The four bands shown in the scheme are consistent with our assignments for oxygen related species at 523 K under cofed ethylene and oxygen (220 cm<sup>-1</sup>, 350 cm<sup>-1</sup>, 600 – 620 cm<sup>-1</sup>, and 800 – 1000 cm<sup>-1</sup> bands from Fig. 2) and  ${\rm Ag_2O}$  nanoparticles (200 – 400 cm<sup>-1</sup>, 620 cm<sup>-1</sup>, and 800 – 1000 cm<sup>-1</sup> bands from Fig. 4). Specifically, features at 200 – 400 cm<sup>-1</sup> arise from surface and subsurface atomic oxygen, broad bands centered near 600 cm<sup>-1</sup> from O–Ag–O motifs, and peaks near 800 – 1000 cm<sup>-1</sup> from dioxygen complexes stabilized by subsurface oxygen, and in the presence of  ${\rm C_2H_4}$  a broad shoulder near 900 cm<sup>-1</sup> and a band near 1570 cm<sup>-1</sup> appear that have previously been assigned to  ${\rm C_2H_4O^*}$ , and  ${\rm C_2H_4^*}$ , respectively.

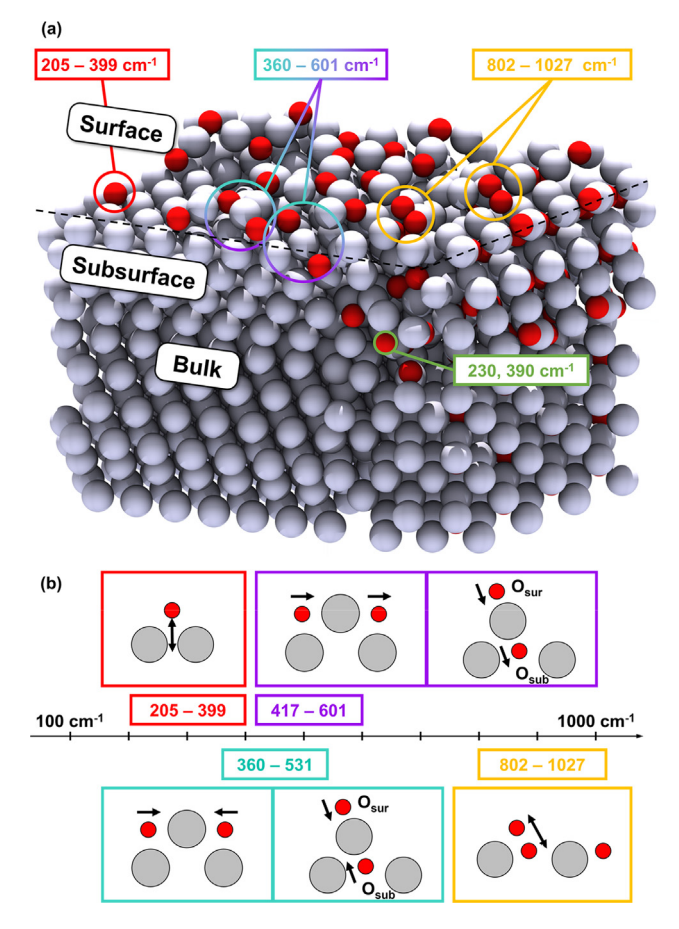


**Fig. 9.** a) Schematic representation of DFT-computed oxygen species (derived from different surfaces) and their vibrational frequencies. The dashed line differentiates surface and subsurface O. b) Depictions of vibrational normal modes and their corresponding ranges of frequencies.

#### $3.6.\ Time\mbox{-Resolved Raman spectra of Ag oxidation and reduction}$

The combined results of in situ Raman spectroscopy, pre- and post-treatment XRD, and computed vibrational frequencies strongly suggest that the Ag nanoparticles form reconstructed surface oxide layers (no more than a few nanometers in thickness) upon oxidative treatments used here. In comparison, the Ag<sub>2</sub>O nanoparticles appear to remain kinetically trapped as bulk oxide structures but undergo restructuring within the near surface region when annealed in O2. Both Ag and Ag2O nanoparticles stabilize O2-derived surface intermediates with Raman features between 800 and 1000 cm<sup>-1</sup> (Fig. 2 and Fig. 4), which in comparison to DFT-derived features suggest that they reflect the presence of diatomic forms of surface oxygen (e.g., peroxides  $(O_2^{2-})$  or superoxides (O<sub>2</sub>)). Together these results indicate that the dioxygen species form exergonically (and do not spontaneously dissociate) provided that the surface and near-surface region already possess near saturation amounts of atomic oxygen. These interpretations suggest a specific chronological sequence for the formation of atomic and diatomic oxygen species on Ag during oxidative treatments and implies the reverse should occur during reduction processes. Spectrokinetic Raman measurements provide an opportunity to directly examine this proposal.

Fig. 10 presents results extracted from time resolved Raman spectra obtained during the initial oxidation of Ag nanoparticles at 473 K (101 kPa  $O_2$ , 2 h) and their subsequent reduction (5 kPa  $H_2$ , 473 K, 8 h), which reveal distinct kinetic behavior of varying populations of surface and subsurface forms of atomic and dia-

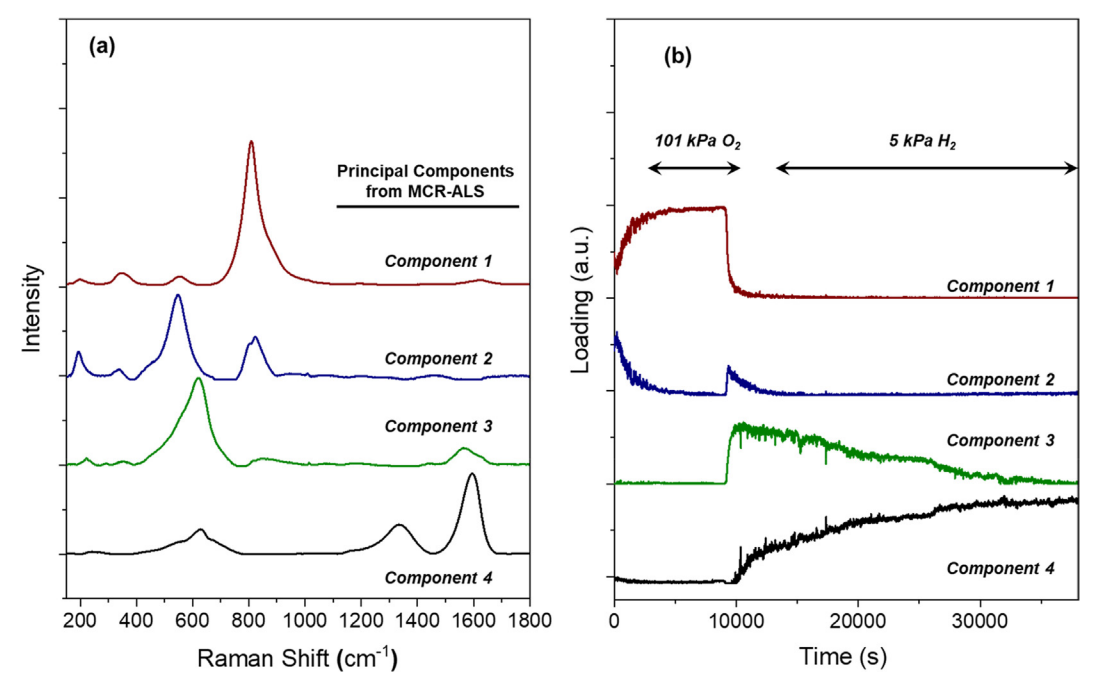


**Fig. 10.** Principal components (a) and corresponding loadings of each component as a function of time (b) obtained from time resolved Raman spectra acquired during an oxidative treatment (101 kPa  $O_2$ , 473 K, 2 h) and followed by a reductive treatment in dilute  $H_2$  (5 kPa  $H_2$ , 473 K, 8 h). Principal components in (a) are attributed to (1) diatomic and atomic oxygen surface intermediates upon highly oxidized Ag surfaces, (2) primarily atomic oxygen in the surface and subsurface region with lesser contributions from diatomic oxygen, (3) surface and subsurface atomic oxygen in reconstructed adlayers, (4) carbonates upon a largely metallic Ag surface. Spectra acquired at 532 nm (0.16 mW μm<sup>-2</sup>) with ~ 5 s time resolution. An oxidative treatment at 773 K (101 kPa  $O_2$ , 4 h) was used to remove all organic residues prior to the experiment.

tomic oxygen and carbonates (CO<sub>3</sub>\*). The loading of component 1, which signifies a combination of surface atomic and diatomic oxygen intermediates, increases and reaches a constant value in the initial stages of the oxidative treatment (2 – 5 ks). During this period, the loadings of all other components are negligible suggesting that the surface and near surface region exists in highly oxidized states (~Ag<sub>2</sub>O) capable of stabilizing the diatomic oxygen species responsible for Raman features between 800 and 1000 cm<sup>-1</sup>. These features can also be supported by the calculated frequencies on Ag<sub>2</sub>O (001) with dioxygen species (Section 3.5 and Fig. 8). Upon contact with  $H_2$  (5 kPa  $H_2$ ,  $\geq$  9 ks), the loading of component 1 attenuates rapidly and becomes negligible at an experimental time of  $\sim 10$  ks. Concomitantly, the loading for component 2 (surface and subsurface atomic oxygen of higher coverage reconstructed adlayers) rises and reaches a maximum by 9.3 ks and subsequently diminishes by 13 ks, which coincides with a slower increase in component 3 (surface and subsurface atomic oxygen of lower coverage reconstructed adlayers) that peaks at 10.5 ks and its gradual decrease until  $\sim$  36 ks. Finally, the intensity of component 4 (carbonates) increases monotonically from 10 to 39 ks, which signifies that these species dominate the surface of the Ag nanoparticles once they are fully reduced. In these and prior experiments, the formation of carbonates in the apparent absence of a C<sub>2</sub>H<sub>4</sub> coreactant must reflect the presence of trace hydrocarbon residues within the gas mixtures used despite use of appropriate adsorbents.

The kinetic behavior of the component loading in Fig. 10b agrees with the proposed assignments for these Raman features in earlier sections (Section 3.2 and Section 3.5). Contact with  $\rm H_2$  consumes diatomic oxygen intermediates upon surface oxides with stoichiometries that resemble  $\rm Ag_2O_1$  more rapidly than any other group of species, either because these diatomic oxygen intermediates react most readily with  $\rm H_2$  or because these species spontaneously dissociate in the presence of oxygen vacancies generated in the  $\rm Ag_2O$ -like surface by reactions with  $\rm H_2$ . Once reactions with

H<sub>2</sub> completely consume diatomic oxygen, further reactions with H<sub>2</sub> necessarily remove atomic oxygen species from the surface and subsurface region and reduce the average coverage of O\*-atoms, which results in changes in the prevailing surface reconstructions. These transitions are represented by the transient growth and attenuation of component 2, which contains features correlating to high and low coverage surface reconstructions but also smaller contributions from  $O_2^{2-}$  complexes that remain in regions of high coverage. Subsequently, coupled diffusion and reaction with H<sub>2</sub> deplete the remaining atomic oxygen species in a much slower process illustrated by the changes in component 3, which largely represents the presence of surface reconstructions that possess lower coverages of O\*-atoms (e.g., those that give the peak near 620 cm<sup>-1</sup>). We attribute this feature to asymmetric vibrations of O-Ag-O motifs located in the surface and subsurface regions. The Raman scattering intensity of these peaks are attenuated when surfaces bind dioxygen species [77] (SI Section S7), become more intense upon reduction and removal of dioxygen surface intermediates, and subsequently are consumed by reaction with H<sub>2</sub> at greater exposure times. The dominance of component 3 (i.e., the 620 cm<sup>-1</sup> feature) at longer times and its slow attenuation during reduction suggests that this low O\*-atoms surface reconstruction persists because the O\*-atoms consumed by reactions with H2 are replenished by solid-state diffusion of additional O\*-atoms from the near-surface region of the Ag nanoparticle. Carbonates (component 4) appear at rates that suggest these species form in regions of the surface with low or negligible coverages of O\*atoms.

These experimental observations agree with the proposal that the Raman features present when pure  $O_2$  contacts Ag and Ag<sub>2</sub>O nanoparticles (Fig. 4) represent diatomic forms of oxygen bound at oxygen vacancies within Ag<sub>2</sub>O (001)-like surfaces (Fig. 8). Wang et al. report that peaks originating at 956 cm<sup>-1</sup> and 800 cm<sup>-1</sup> give rise to new peaks at  $\sim 931$  cm<sup>-1</sup> and  $\sim 778$  cm<sup>-1</sup> upon replacement of  $^{16}O_2$  with  $^{18}O_2$ , resulting in a 20 – 24 cm<sup>-1</sup> shift [59], which

resembles similar reports of  $\sim 20~\text{cm}^{-1}$  isotopic shifts for bands in the  $800 - 1000 \,\mathrm{cm}^{-1}$  by other groups [74,108]. These shifts appear inconsistent with prior studies that interpreted these differences as evidence that observed features at 800 - 1000 cm<sup>-1</sup> reflected different forms of atomic oxygen. In comparison, molecularly adsorbed  $O_2$  on metallic Ag exhibits a  $\sim 55~\text{cm}^{-1}$  isotopic shift but desorbs at temperatures > 380 K [106,107,115,145]. We calculated differences between  $\nu(Ag^{-16}O_2)$  and  $\nu(Ag^{-18}O_2)$  for all the diatomic oxygen species depicted in Fig. 8 and determined these values range from 52 to 59 cm<sup>-1</sup>. However, the dioxygen structures may form both by direct adsorption of O<sub>2</sub> but also surface reactions that reform O-O bonds among atomic species at 523 K in Fig. 8 and Fig. 9. Therefore, past measurements likely reflect the presence of diatomic <sup>16</sup>O<sup>18</sup>O derived from reactions among <sup>16</sup>O<sub>2</sub> and <sup>18</sup>O<sub>2</sub> and atomic forms of <sup>16</sup>O or <sup>18</sup>O. Upon the highly oxidized Ag surfaces depicted in Fig. 8, the computed frequency difference between v $(Ag^{-16}O^{-16}O)$  and  $v(Ag^{-18}O^{-16}O)$  range from 24 to 29 cm<sup>-1</sup>, similar to the widely reported  $\sim 20\ \text{cm}^{-1}$  isotopic shift observed by several groups under similar conditions [19,19,74,108]. This scenario may involve reversible formation of  $O_{surface} = O_{subsurface}$  complexes proposed to be responsible for the  $\sim 800~cm^{-1}$  band and discussed in a recent review from Pu et al. [19]. The computed frequencies for exergonic forms of O2\* and experimental frequencies occupy a broad range between 800 and 1000 cm<sup>-1</sup> that reflect a strong dependence on the binding site, the relative coverage of atomic and diatomic coadsorbates, and presumably the surface structure of the oxide-film modeled as Ag<sub>2</sub>O. Consequently, we conclude that the previously measured experimental shifts in features following isotope substitution may be consistent with certain configurations of O2\* species that form on oxide-like films encapsulating Ag nanoparticles.

#### 4. Conclusions

Surface structure and reactive intermediates formed by contact between Ag nanoparticles and mixtures of O<sub>2</sub> and C<sub>2</sub>H<sub>4</sub> influence rates and selectivities for ethylene epoxidation and their determination requires experimental and computational methods that are capable of examining the form of the surface that exists during catalysis. Here, we provide compelling evidence from in situ SERS spectra (acquired at steady-state and during transients) and ab initio free energy and frequency calculations that suggest significant fractions of the surfaces of Ag particles form reconstructed surface oxides and stabilize diatomic oxygen during EO catalysis. These reconstructed and Ag-oxide-like surfaces are represented by O-Ag-O structural motifs that appear as a broad Raman scattering feature centered near  $600~\text{cm}^{-1}$ . This feature decreases as  $O_2$  to C<sub>2</sub>H<sub>4</sub> ratios increase due to the formation of diatomic oxygen on the surface and an increase in the amount of subsurface oxygen, which decreases the Raman scattering intensity of these vibrations [77]. We assign the band centered near 810 – 840 cm<sup>-1</sup> to dioxygen complexes composed of surface and lattice O that form on an oxide-like overlayer during both exposure to O2 and steadystate reaction. Unlike molecular oxygen adsorbed on metallic Ag, these dioxygen complexes are stable at temperatures representative of EO catalysis (473 – 573 K) and form only after the Ag surface contains substantial contents of surface and subsurface O. Our interpretations differ from longstanding proposals that the features centered near 800 cm<sup>-1</sup> on Ag represented atomic oxygen species, although the assignments for these features were never resolved in prior studies.

The ubiquitous appearance of the same Raman bands on EO catalysts composed of single crystal and supported and unsupported polycrystalline particles is consistent with the proposal that the Ag surface undergoes oxidation and reconstruction to resemble a

surface oxide during EO catalysis. This oxide layer is thicker than the Ag<sub>2</sub>O tri-layer surfaces considered in prior literature, and while its exact structure remains unknown, our results highlight a need for identification of the molecular structure of Ag-oxide films beyond previously proposed reconstructions. We rationalize foundational and recent observations of structure insensitivity of ethylene oxidation rates to be a consequence of surface saturation and reconstruction, as proposed by Boudart. This view agrees with a recent report from van Hoof et al. [18] that evidences oxygen diffusion and dissolution into Ag particles under reactions conditions that leads to ethylene oxidation rates normalized to the surface area of the first outer shell of crystallites that are independent of particle size. Informed by these realizations, further research aims to relate the structure of the surface oxide and the number of oxygen vacancies to rates and selectivities for ethylene epoxidation using in operando methods and ab initio calculations.

#### **Declaration of Competing Interest**

The authors declare that they have no known competing financial interests or personal relationships that could have appeared to influence the work reported in this paper.

#### Acknowledgment

The authors acknowledge Research Computing at the University of Virginia for providing computational resources and technical support that have contributed to the results reported within this publication. D.W.F., D.P.W., C.P., A.S. and C.L. acknowledge funding provided by the National Science Foundation (CBET-1942015). This research was carried out in part in the Materials Research Laboratory Central Research Facilities, University of Illinois.

#### Appendix A. Supplementary data

Supplementary data to this article can be found online at https://doi.org/10.1016/j.jcat.2021.11.031.

#### References

- [1] M. Boudart, Chemisorption during catalytic reaction on metal surfaces, J. Vac. Sci. Technol. 12 (1) (1975) 329–332.
- [2] M. Boudart, Turnover Rates in Heterogeneous Catalysis, Chem. Rev. 95 (3) (1995) 661–666.
- [3] M. Boudart, Classical catalytic kinetics: a placebo or the real thing?, Ind. Eng. Chem. Fundam. 25 (4) (1986) 656–658.
- [4] J.A. Dumesic, H. Topsøe, S. Khammouma, M. Boudart, Surface, catalytic and magnetic properties of small iron particles: II. Structure sensitivity of ammonia synthesis, J. Catal. 37 (1975) 503–512.
- [5] J.A. Dumesic, H. Topsøe, M. Boudart, Surface, catalytic and magnetic properties of small iron particles: III. Nitrogen induced surface reconstruction, J. Catal. 37 (1975) 513–522.
- [6] N.D. Spencer, R.C. Schoonmaker, G.A. Somorjai, Iron single crystals as ammonia synthesis catalysts: Effect of surface structure on catalyst activity, J. Catal. 74 (1982) 129–135.
- [7] H. Hirano, K.-I. Tanaka, A reason for the structure-insensitive catalytic activity of Ni(100) and Ni(111) surfaces for the methanation reaction of CO, J. Catal. 133 (1992) 461–466.
- [8] M.E. Bussel, A.J. Gellman, G.A. Somorjai, The role of adsorbate overlayers in thiophene hydrodesulfurization over molybdenum and rhenium single crystals, Catal. Lett. 1 (6-7) (1988) 195–201.
- [9] S.J. Thomson, G. Webb, Catalytic hydrogenation of olefins on metals: a new interpretation, J. Chem. Soc. Chem. Commun. (13) (1976) 526.
- [10] M. Boudart, A. Aldag, J.E. Benson, N.A. Dougharty, C. Girvin Harkins, On the specific activity of platinum catalysts, J. Catal. 6 (1) (1966) 92–99.
- [11] M. Boudart, Catalysis by Supported Metals\*\*This work was sponsored by grant CK 648 of the National Science Foundation. Its continuity over the years has been assured by a generous grant from the Petroleum Research Fund of the American Chemical Society, in: D.D. Eley, H. Pines, P.B. Weisz (Eds.), Adv, Academic Press, Catal., 1969, pp. 153–166.
- [12] M. Boudart, G. Djega-Mariadassou, Kinetics of Heterogeneous Catalytic Reactions, Princeton University Press, 2014.

- [13] D.J. Sajkowski, M. Boudart, Structure Sensitivity of the Catalytic Oxidation of Ethene by Silver, Catal. Rev. 29 (4) (1987) 325–360.
- [14] M. Boudart, in: Proc. 5th International Congr. Catal., The Chemical Society, London, 1976: p. 1.
- [15] C.T. Campbell, The selective epoxidation of ethylene catalyzed by Ag(111): A comparison with Ag(110), J. Catal. 94 (1985) 436–444.
- [16] C.T. Campbell, B.E. Koel, Chlorine promotion of selective ethylene oxidation over Ag(110): Kinetics and mechanism, J. Catal. 92 (1985) 272–283.
- [17] R.B. Grant, R.M. Lambert, A single crystal study of the silver-catalysed selective oxidation and total oxidation of ethylene, J. Catal. 92 (1985) 364– 375
- [18] A.J.F. van Hoof, E.A.R. Hermans, A.P. van Bavel, H. Friedrich, E.J.M. Hensen, Structure Sensitivity of Silver-Catalyzed Ethylene Epoxidation, ACS Catal. 9 (11) (2019) 9829–9839.
- [19] Tiancheng Pu, Huijie Tian, Michael E. Ford, Srinivas Rangarajan, Israel E. Wachs, Overview of Selective Oxidation of Ethylene to Ethylene Oxide by Ag Catalysts, ACS Catal. 9 (12) (2019) 10727–10750.
- [20] J.E. van den Reijen, S. Kanungo, T.A.J. Welling, M. Versluijs-Helder, T.A. Nijhuis, K.P. de Jong, P.E. de Jongh, Preparation and particle size effects of Ag/ α-Al2O3 catalysts for ethylene epoxidation, J. Catal. 356 (2017) 65–74.
- [21] Weijian Diao, Christopher D. DiGiulio, Melanie T. Schaal, Shuguo Ma, John R. Monnier, An investigation on the role of Re as a promoter in AgCsRe/α-Al2O3 high-selectivity, ethylene epoxidation catalysts, J. Catal. 322 (2015) 14–23.
- [22] Cha-Jung Chen, James W. Harris, Aditya Bhan, Kinetics of Ethylene Epoxidation on a Promoted Ag/α-Al2O3 Catalyst—The Effects of Product and Chloride Co-Feeds on Rates and Selectivity, Chem. – Eur. J. 24 (47) (2018) 12405–12415.
- [23] James W. Harris, Jeffrey A. Herron, Joseph F. DeWilde, Aditya Bhan, Molecular characteristics governing chlorine deposition and removal on promoted Ag catalysts during ethylene epoxidation, J. Catal. 377 (2019) 378–388.
- [24] James W. Harris, Aditya Bhan, Kinetics of chlorine deposition and removal over promoted silver catalysts during ethylene epoxidation, J. Catal. 380 (2019) 318–331.
- [25] James W. Harris, Aditya Bhan, Moderation of chlorine coverage and ethylene epoxidation kinetics via ethane oxychlorination over promoted Ag/ $\alpha$ -Al2O3, J. Catal. 367 (2018) 62–71.
- [26] H. Xu, L. Zhu, Y. Nan, Y. Xie, D. Cheng, Revisit the Role of Metal Dopants in Enhancing the Selectivity of Ag-Catalyzed Ethylene Epoxidation: Optimizing Oxophilicity of Reaction Site via Cocatalytic Mechanism, ACS Catal. 11 (2021) 3371–3383.
- [27] Haoxiang Xu, Lin Zhu, Yang Nan, Yuan Xie, Daojian Cheng, Revisit the Role of Chlorine in Selectivity Enhancement of Ethylene Epoxidation, Ind. Eng. Chem. Res. 58 (47) (2019) 21403–21412.
- [28] Zhenhao Li, Lin Zhu, Jian-Feng Chen, Daojian Cheng, Enhanced Ethylene Oxide Selectivity by Cu and Re Dual-Promoted Ag Catalysts, Ind. Eng. Chem. Res. 57 (12) (2018) 4180–4185.
- [29] V.I. Bukhtiyarov, A. Knop-Gericke, Chapter 9. Ethylene Epoxidation over Silver Catalysts, in: C. Hess, R. Schlögl (Eds.), Nanosci, Royal Society of Chemistry, Cambridge, Nanotechnol. Ser., 2011, pp. 214–247.
- [30] U.E.N.C. for E. Assessment, Ethylene glycol, (2009).
- [31] P. Christopher, S. Linic, Engineering Selectivity in Heterogeneous Catalysis: Ag Nanowires as Selective Ethylene Epoxidation Catalysts, J. Am. Chem. Soc. 130 (2008) 11264–11265.
- [32] M.O. Ozbek, I. Onal, R.A. Van Santen, Ethylene epoxidation catalyzed by chlorine-promoted silver oxide, J. Phys. Condens. Matter Inst. Phys. J. 23 (2011) 404202.
- [33] M. Oluş Özbek, Işik Önal, Rutger A. van Santen, Chlorine and Caesium Promotion of Silver Ethylene Epoxidation Catalysts, ChemCatChem. 5 (2) (2013) 443–451.
- [34] Suljo Linic, Mark A. Barteau, On the Mechanism of Cs Promotion in Ethylene Epoxidation on Ag, J. Am. Chem. Soc. 126 (26) (2004) 8086–8087.
- [35] M. Olus Özbek, Isik Önal, Rutger A. van Santen, Ethylene Epoxidation Catalyzed by Silver Oxide, ChemCatChem. 3 (1) (2011) 150–153.
- [36] M.O. Ozbek, I. Onal, R.A. van Santen, Effect of Surface and Oxygen Coverage on Ethylene Epoxidation, Top. Catal. 55 (11-13) (2012) 710-717.
- [37] M.O. Ozbek, I. Onal, R.A. van Santen, Why silver is the unique catalyst for ethylene epoxidation, J. Catal. 284 (2) (2011) 230–235.
- [38] M.A. Barteau, New Perspectives on Direct Heterogeneous Olefin Epoxidation, Top. Catal. 22 (2003) 3–8.
- [39] Suljo Linic, Mark A. Barteau, Control of Ethylene Epoxidation Selectivity by Surface Oxametallacycles, J. Am. Chem. Soc. 125 (14) (2003) 4034–4035.
- [40] Phillip Christopher, Suljo Linic, Shape- and Size-Specific Chemistry of Ag Nanostructures in Catalytic Ethylene Epoxidation, ChemCatChem. 2 (1) (2010) 78–83.
- [41] Suljo Linic, Mark A. Barteau, Formation of a Stable Surface Oxametallacycle that Produces Ethylene Oxide, J. Am. Chem. Soc. 124 (2) (2002) 310–317.
- [42] S. Linic, H. Piao, K. Adib, M.A. Barteau, Ethylene Epoxidation on Ag: Identification of the Crucial Surface Intermediate by Experimental and Theoretical Investigation of its Electronic Structure, Angew. Chem. 116 (2004) 2978–2981.
- [43] S. Linic, M.A. Barteau, Construction of a reaction coordinate and a microkinetic model for ethylene epoxidation on silver from DFT calculations and surface science experiments, J. Catal. 214 (2003) 200–212.
- [44] Suljo Linic, Jerome Jankowiak, Mark A. Barteau, Selectivity driven design of bimetallic ethylene epoxidation catalysts from first principles, J. Catal. 224 (2) (2004) 489–493.

- [45] M.F. Fellah, R.A. van Santen, I. Onal, Epoxidation of Ethylene by Silver Oxide (Ag2O) Cluster: A Density Functional Theory Study, Catal. Lett. 141 (2011) 762–771
- [46] P.J. Van den Hoek, E.J. Baerends, R.A. Van Santen, Ethylene epoxidation on silver(110): the role of subsurface oxygen, J. Phys. Chem. 93 (1989) 6469– 6475
- [47] N.W. Cant, W.K. Hall, Catalytic oxidation: VI. Oxidation of labeled olefins over silver, J. Catal. 52 (1978) 81–94.
- [48] W.M.H. Sachtler, C. Backx, R.A. Van Santen, On the Mechanism of Ethylene Epoxidation, Catal. Rev. 23 (1-2) (1981) 127–149.
- [49] R.A. Van Santen, H.P.C.E. Kuipers, The Mechanism of Ethylene Epoxidation, in: D.D. Eley, H. Pines, P.B. Weisz (Eds.), Adv, Academic Press, Catal., 1987, pp. 265–321.
- [50] Charles T. Campbell, Mark T. Paffett, The interactions of O2, CO and CO2 with Ag(110), Surf. Sci. 143 (2-3) (1984) 517–535.
- [51] C.T. Campbell, M.T. Paffett, Model studies of ethylene epoxidation catalyzed by the Ag(110) surface, Surf. Sci. 139 (2–3) (1984) 396–416.
- [52] C. Stegelmann, N.C. Schiødt, C.T. Campbell, P. Stoltze, Microkinetic modeling of ethylene oxidation over silver, J. Catal. 221 (2) (2004) 630–649.
- [53] Robert B. Grant, Richard M. Lambert, Mechanism of the silver-catalysed heterogeneous epoxidation of ethylene, J. Chem. Soc. Chem. Commun. (12) (1983) 662.
- [54] Federico J. Williams, Daniel P.C. Bird, Alejandra Palermo, Ashok K. Santra, Richard M. Lambert, Mechanism, Selectivity Promotion, and New Ultraselective Pathways in Ag-Catalyzed Heterogeneous Epoxidation, J. Am. Chem. Soc. 126 (27) (2004) 8509–8514.
- [55] M.M. Montemore, M.A. van Spronsen, R.J. Madix, C.M. Friend, O<sub>2</sub> Activation by Metal Surfaces: Implications for Bonding and Reactivity on Heterogeneous Catalysts, Chem. Rev. 118 (2018) 2816–2862.
- [56] Arno J.F. van Hoof, Ivo A.W. Filot, Heiner Friedrich, Emiel J.M. Hensen, Reversible Restructuring of Silver Particles during Ethylene Epoxidation, ACS Catal. 8 (12) (2018) 11794–11800.
- [57] Jonathan Derouin, Rachael G. Farber, Marie E. Turano, Erin V. Iski, Daniel R. Killelea, Thermally Selective Formation of Subsurface Oxygen in Ag(111) and Consequent Surface Structure, ACS Catal. 6 (7) (2016) 4640–4646.
- [58] N.M. Martin, S. Klacar, H. Grönbeck, J. Knudsen, J. Schnadt, S. Blomberg, J. Gustafson, E. Lundgren, High-coverage oxygen-induced surface structures on Ag(111), J. Phys. Chem. C. 118 (28) (2014) 15324–15331.
- [59] C.-B. Wang, G. Deo, I.E. Wachs, Interaction of Polycrystalline Silver with Oxygen, Water, Carbon Dioxide, Ethylene, and Methanol. In Situ Raman and Catalytic Studies, J. Phys. Chem. B. 103 (1999) 5645–5656.
- [60] A. Reicho, A. Stierle, I. Costina, H. Dosch, Stranski-Krastanov like oxide growth on Ag(1 1 1) at atmospheric oxygen pressures, Surf. Sci. 601 (4) (2007) L19-
- [61] B. Pettinger, X. Bao, I.C. Wilcock, M. Muhler, G. Ertl, Surface-enhanced Raman scattering from surface and subsurface oxygen species at microscopically well-defined Ag surfaces, Phys. Rev. Lett. 72 (10) (1994) 1561–1564.
- [62] Jonathan Derouin, Rachael G. Farber, Stacy L. Heslop, Daniel R. Killelea, Formation of surface oxides and Ag2O thin films with atomic oxygen on Ag (111), Surf. Sci. 641 (2015) L1–L4.
- [63] Ye Xu, Jeff Greeley, Manos Mavrikakis, Effect of Subsurface Oxygen on the Reactivity of the Ag(111) Surface, J. Am. Chem. Soc. 127 (37) (2005) 12823– 12827
- [64] Emilia A. Carbonio, Tulio C.R. Rocha, Alexander Yu. Klyushin, Igor Píš, Elena Magnano, Silvia Nappini, Simone Piccinin, Axel Knop-Gericke, Robert Schlögl, Travis E. Jones, Are multiple oxygen species selective in ethylene epoxidation on silver?, Chem. Sci. 9 (4) (2018) 990–998.
- [65] T.C.R. Rocha, A. Oestereich, D.V. Demidov, M. Hävecker, S. Zafeiratos, G. Weinberg, V.I. Bukhtiyarov, A. Knop-Gericke, R. Schlögl, The silver-oxygen system in catalysis: new insights by near ambient pressure X-ray photoelectron spectroscopy, Phys. Chem. Chem. Phys. 14 (2012) 4554-4564
- [66] Travis E. Jones, Regina Wyrwich, Sebastian Böcklein, Tulio C.R. Rocha, Emilia A. Carbonio, Axel Knop-Gericke, Robert Schlögl, Sebastian Günther, Joost Wintterlin, Simone Piccinin, Oxidation of Ethylene on Oxygen Reconstructed Silver Surfaces, J. Phys. Chem. C. 120 (50) (2016) 28630–28638.
- [67] T.C.R. Rocha, M. Hävecker, A. Knop-Gericke, R. Schlögl, Promoters in heterogeneous catalysis: The role of Cl on ethylene epoxidation over Ag, J. Catal. 312 (2014) 12–16.
- [68] Matthew M. Montemore, J.Will Medlin, Predicting and Comparing C-M and O-M Bond Strengths for Adsorption on Transition Metal Surfaces, J. Phys. Chem. C. 118 (5) (2014) 2666–2672.
- [69] P.H. McBreen, M. Moskovits, A surface-enhanced Raman study of ethylene and oxygen interacting with supported silver catalysts, J. Catal. 103 (1987) 188–199
- [70] E.L. Force, A.T. Bell, Infrared spectra of adsorbed species present during the oxidation of ethylene over silver, J. Catal. 38 (1975) 440–460.
- [71] Wang Xiao-Dong, W.T. Tysoe, Robert G. Greenler, K. Truszkowska, A reflection-absorption infrared spectroscopy study of the adsorption of atomic oxygen on silver, Surf. Sci. 257 (1-3) (1991) 335–343.
- [72] Angeles Pulido, Patricia Concepción, Mercedes Boronat, Avelino Corma, Aerobic epoxidation of propene over silver (111) and (100) facet catalysts, J. Catal. 292 (2012) 138–147.
- [73] G.I.N. Waterhouse, G.A. Bowmaker, J.B. Metson, Oxygen chemisorption on an electrolytic silver catalyst: a combined TPD and Raman spectroscopic study, Appl. Surf. Sci. 214 (2003) 36–51.

- [74] D.I. Kondarides, G.N. Papatheodorou, C.G. Vayenas, X.E. Verykios, In Situ High Temperature SERS Study of Oxygen Adsorbed on Ag: Support and Electrochemical Promotion Effects, Berichte Bunsenges. Für Phys. Chem. 97 (1993) 709–719.
- [75] Jingfa Deng, Xinhua Xu, Jinhai Wang, Yuanyan Liao, Bifeng Hong, In situ surface Raman spectroscopy studies of oxygen adsorbed on electrolytic silver, Catal. Lett. 32 (1-2) (1995) 159–170.
- [76] X. Bao, B. Pettinger, G. Ertl, R. Schlögl, In-situ Raman Studies of Ethylene Oxidation at Ag(111) and Ag(110) under Catalytic Reaction Conditions, Berichte Bunsenges. Für Phys. Chem. 97 (3) (1993) 322–325.
- [77] B. Pettinger, X. Bao, I. Wilcock, M. Muhler, R. Schlögl, G. Ertl, Thermal Decomposition of Silver Oxide Monitored by Raman Spectroscopy: From AgO Units to Oxygen Atoms Chemisorbed on the Silver Surface, Angew. Chem. Int. Ed. Engl. 33 (1994) 85–86.
- [78] X. Bao, M. Muhler, B. Pettinger, Y. Uchida, G. Lehmpfuhl, R. Schlögl, G. Ertl, The effect of water on the formation of strongly bound oxygen on silver surfaces, Catal. Lett. 32 (1995) 171–183.
- [79] X. Bao, M. Muhler, B. Pettinger, R. Schlögl, G. Ertl, On the nature of the active state of silver during catalytic oxidation of methanol, Catal. Lett. 22 (1993) 215–225.
- [80] V BUKHTIYAROV, A NIZOVSKII, H BLUHM, M HAVECKER, E KLEIMENOV, A KNOPGERICKE, R SCHLOGL, Combined in situ XPS and PTRMS study of ethylene epoxidation over silver, J. Catal. 238 (2) (2006) 260–269.
- [81] N.G. Bastús, F. Merkoçi, J. Piella, V. Puntes, Synthesis of Highly Monodisperse Citrate-Stabilized Silver Nanoparticles of up to 200 nm: Kinetic Control and Catalytic Properties, Chem. Mater. 26 (2014) 2836–2846.
- [82] Joaquim Jaumot, Raimundo Gargallo, Anna de Juan, Romà Tauler, A graphical user-friendly interface for MCR-ALS: a new tool for multivariate curve resolution in MATLAB, Chemom. Intell. Lab. Syst. 76 (1) (2005) 101–110.
- [83] G. Kresse, J. Furthmüller, Efficient iterative schemes for ab initio total-energy calculations using a plane-wave basis set, Phys Rev B. 54 (16) (1996) 11169–11186
- [84] John P. Perdew, Yue Wang, Accurate and simple analytic representation of the electron-gas correlation energy, Phys Rev B. 45 (23) (1992) 13244– 13249
- [85] P.E. Blöchl, Projector augmented-wave method, Phys. Rev. B. 50 (24) (1994) 17953–17979.
- [86] G. Kresse, D. Joubert, From ultrasoft pseudopotentials to the projector augmented-wave method, Phys. Rev. B. 59 (1999) 1758.
- [87] A. Jain, S.P. Ong, G. Hautier, W. Chen, W.D. Richards, S. Dacek, S. Cholia, D. Gunter, D. Skinner, G. Ceder, K. a. Persson, The Materials Project: A materials genome approach to accelerating materials innovation, APL Mater. 1 (2013) 11002.
- [88] A.H. Larsen, J.J. Mortensen, J. Blomqvist, I.E. Castelli, R. Christensen, M. Dulak, J. Friis, M.N. Groves, B. Hammer, C. Hargus, E.D. Hermes, P.C. Jennings, P.B. Jensen, J. Kermode, J.R. Kitchin, E.L. Kolsbjerg, J. Kubal, K. Kaasbjerg, S. Lysgaard, J.B. Maronsson, T. Maxson, T. Olsen, L. Pastewka, A. Peterson, C. Rostgaard, J. Schiøtz, O. Schiüt, M. Strange, K.S. Thygesen, T. Vegge, L. Vilhelmsen, M. Walter, Z. Zeng, K.W. Jacobsen, The atomic simulation environment—a Python library for working with atoms, J. Phys. Condens. Matter. 29 (2017) 273002.
- [89] S.P. Ong, W.D. Richards, A. Jain, G. Hautier, M. Kocher, S. Cholia, D. Gunter, V.L. Chevrier, K.A. Persson, G. Ceder, Python Materials Genomics (pymatgen): A robust, open-source python library for materials analysis, Comput. Mater. Sci. 68 (2013) 314–319.
- [90] Jacob R. Boes, John R. Kitchin, Neural network predictions of oxygen interactions on a dynamic Pd surface, Mol. Simul. 43 (5-6) (2017) 346–354.
- [91] Jacob R. Boes, Osman Mamun, Kirsten Winther, Thomas Bligaard, Graph Theory Approach to High-Throughput Surface Adsorption Structure Generation, J. Phys. Chem. A. 123 (11) (2019) 2281–2285.
- [92] D. McQuarrie, Statistical mechanics university science books, Sausalito CA. (2000) 222–223.
- [93] M.W. Chase, C.A. Davies, J.R. Downey, D.J. Frurip, R.A. McDonald, A.N. Syverud, NIST JANAF Thermochemical Tables ver. 1.0, US Dept Commer. (1985).
   [94] H.E. Swanson, M.C. Morris, R.P. Stinchfield, E.H. Evans, Standard X-ray
- [94] H.E. Swanson, M.C. Morris, R.P. Stinchfield, E.H. Evans, Standard X-ray Diffraction Powder Patterns: Section 1. Data for 46 Substances, UNT Digit, Libr. (1962).
- [95] N. Yuantao, Z. Xinmin, D. Hong, Chin. J. Met. Sci. Technol. 7 (1991) 391.
- [96] J Spreadborough, J W Christian, High-temperature X-ray diffractometer, J. Sci. Instrum. 36 (3) (1959) 116–118.
- [97] Travis E. Jones, Tulio C.R. Rocha, Axel Knop-Gericke, Catherine Stampfl, Robert Schlögl, Simone Piccinin, Insights into the Electronic Structure of the Oxygen Species Active in Alkene Epoxidation on Silver, ACS Catal. 5 (10) (2015) 5846– 5850
- [98] E. Force, A.T. Bell, The relationship of adsorbed species observed by infrared spectroscopy to the mechanism of ethylene oxidation over silver, J. Catal. 40 (1975) 356–371.
- [99] D Stacchiola, G Wu, M Kaltchev, W.T Tysoe, A reflection-absorption infrared spectroscopic study of the adsorption of ethylene and ethylene oxide on oxygen-covered Ag(111), Surf. Sci. 486 (1-2) (2001) 9–23.
- [100] D. Lin-Vien, N.B. Colthup, W.G. Fateley, J.G. Grasselli, The handbook of infrared and Raman characteristic frequencies of organic molecules, Elsevier, (1991).
- [101] R. Abdallah, T. Mäurer, T. Rosendahl, F. Rosowski, G. Theis T. Mazanec, S. Deshmukh, L.J. Silva. Process for making ethylene oxide. U.S. Patent 8 933: (2015) 254.

- [102] L. Zhang, R.R. Tupe, A.G. Phillips, P.V. Hinman, H. Soo. Dow Technology Investments LLC, Process for conditioning a high efficiency ethylene oxide catalyst. U.S. Patent 8 815: (2014) 769.
- [103] B.A. Sexton, R.J. Madix, Vibrational spectra of molecular and atomic oxygen on Ag(110), Chem. Phys. Lett. 76 (1980) 294–297.
- [104] K Prabhakaran, C.N.R Rao, A combined EELS-XPS study of molecularly chemisorbed oxygen on silver surfaces: Evidence for superoxo and peroxo species, Surf. Sci. Lett. 186 (3) (1987) 575–580.
- [105] G.I.N. Waterhouse, G.A. Bowmaker, J.B. Metson, The thermal decomposition of silver (I, III) oxide: A combined XRD, FT-IR and Raman spectroscopic study, Phys. Chem. Chem. Phys. 3 (2001) 3838–3845.
- [106] Xiao-Dong Wang, Robert G. Greenler, Direct structure determination of oxygen adsorbed on silver by reflection-absorption infrared spectroscopy with isotopic substitution, Phys. Rev. B. 43 (8) (1991) 6808–6811.
- [107] C. Pettenkofer, I. Pockrand, A. Otto, Surface enhanced Raman spectra of oxygen adsorbed on silver, Surf. Sci. 135 (1-3) (1983) 52-64.
- [108] Graeme J. Millar, James B. Metson, Graham A. Bowmaker, Ralph P. Cooney, In situ Raman studies of the selective oxidation of methanol to formaldehyde and ethene to ethylene oxide on a polycrystalline silver catalyst, J. Chem. Soc. Faraday Trans. 91 (22) (1995) 4149.
- [109] I. Pockrand, Surface-enhanced Raman scattering from evaporated Ag films: Influence of adsorbate and annealing on excitation spectra, Chem. Phys. Lett. 92 (1982) 514–518.
- [110] J.L. Carter, D.J.C. Yates, P.J. Lucchesi, J.J. Elliott, V. Kevorkian, The Adsorption of Ethylene on a Series of Near-Faujasite Zeolites Studied by Infrared Spectroscopy and Calorimetry, J. Phys. Chem. 70 (4) (1966) 1126–1136.
- [111] T. Shimanouchi, Tables of molecular vibrational frequencies, US Government Printing Office (1973).
- [112] M.E. Witzke, A. Almithn, C.L. Conrad, M.D. Triezenberg, D.D. Hibbitts, D.W. Flaherty, In Situ Methods for Identifying Reactive Surface Intermediates during Hydrogenolysis Reactions: C-O Bond Cleavage on Nanoparticles of Nickel and Nickel Phosphides, J. Am. Chem. Soc. 141 (2019) 16671–16684.
- [113] A. Urakawa, T. Bürgi, A. Baiker, Sensitivity enhancement and dynamic behavior analysis by modulation excitation spectroscopy: Principle and application in heterogeneous catalysis, Chem. Eng. Sci. 63 (2008) 4902–4909.
- [114] A.W Czanderna, The interaction of carbon dioxide and ethane with silver, J. Colloid Interface Sci. 22 (5) (1966) 482–490.
- [115] C.T. Campbell, Atomic and molecular oxygen adsorption on Ag(111), Surf. Sci. 157 (1) (1985) 43–60.
- [116] C. Backx, C.P.M. De Groot, P. Biloen, W.M.H. Sachtler, Interaction of O2, CO2, CO, C2H4 and C2H4O with Ag(110), Surf. Sci. 128 (1) (1983) 81–103.
- [117] P.A. Kilty, W.M.H. Sachtler, The mechanism of the selective oxidation of ethylene to ethylene oxide, Catal. Rev. 10 (1) (1974) 1–16.
- [118] M.O. Özbek, R.A. van Santen, The Mechanism of Ethylene Epoxidation Catalysis, Catal. Lett. 143 (2) (2013) 131–141.
- [119] Travis E. Jones, Tulio C.R. Rocha, Axel Knop-Gericke, Catherine Stampfl, Robert Schlögl, Simone Piccinin, Thermodynamic and spectroscopic properties of oxygen on silver under an oxygen atmosphere, Phys. Chem. Chem. Phys. 17 (14) (2015) 9288-9312.
- [120] Graeme J. Millar, James B. Metson, Graham A. Bowmaker, Ralph P. Cooney, Influence of oxidation and reduction conditions upon the morphology of silica-supported polycrystalline silver catalysts, J. Chem. Soc. Faraday Trans. 91 (1) (1995) 133.
- [121] Kai Liu, Tao Chen, Shuyue He, Jason P. Robbins, Simon G. Podkolzin, Fei Tian, Observation and Identification of an Atomic Oxygen Structure on Catalytic Gold Nanoparticles, Angew. Chem. 129 (42) (2017) 13132–13137.
  [122] W.A. Parkhurst, S. Dallek, B.F. Larrick, Thermogravimetry-Evolved Gas
- [122] W.A. Parkhurst, S. Dallek, B.F. Larrick, Thermogravimetry-Evolved Gas Analysis of Silver Oxide Cathode Material, J. Electrochem. Soc. 131 (1984) 1739
- [123] Issei Nakamori, Hidetsugu Nakamura, Toshiyuki Hayano, Shuichi Kagawa, The Thermal Decomposition and Reduction of Silver(I) Oxide, Bull. Chem. Soc. Jpn. 47 (8) (1974) 1827–1832.
- [124] C.I. Carlisle, D.A. King, M.L. Bocquet, J. Cerdá, P. Sautet, Imaging the surface and the interface atoms of an oxide film on Ag(111) by scanning tunneling microscopy: Experiment and theory, Phys. Rev. Lett. 84 (2000) 3899–3902.
- [125] J. Schnadt, A. Michaelides, J. Knudsen, R.T. Vang, K. Reuter, E. Lægsgaard, M. Scheffler, F. Besenbacher, Revisiting the structure of the p(4×4) surface oxide on Ag(111), Phys. Rev. Lett. 96 (2006) 4–7.
- [126] M. Schmid, A. Reicho, A. Stierle, I. Costina, J. Klikovits, P. Kostelnik, O. Dubay, G. Kresse, J. Gustafson, E. Lundgren, J.N. Andersen, H. Dosch, P. Varga, Structure of Ag(111)-p(4×4)-O: No silver oxide, Phys. Rev. Lett. 96 (2006) 1-
- [127] Angelos Michaelides, Karsten Reuter, Matthias Scheffler, When seeing is not believing: Oxygen on Ag(111), a simple adsorption system?, J. Vac. Sci. Technol. Vac. Surf. Films. 23 (6) (2005) 1487–1497.
- [128] Robert B. Wexler, Tian Qiu, Andrew M. Rappe, Automatic Prediction of Surface Phase Diagrams Using Ab, Initio Grand Canonical Monte Carlo 123 (4) (2019) 2321–2328.
- [129] C.T. Campbell, Transition Metal Oxides: Extra Thermodynamic Stability as Thin Films, Phys. Rev. Lett. 96 (2006) 23–26.
- [130] J. Assal, B. Hallstedt, L.J. Gauckler, Thermodynamic Assessment of the Silver-Oxygen System, J. Am. Ceram. Soc. 80 (1997) 3054–3060.
- [131] I. Karakaya, W.T. Thompson, The Ag-O (silver-oxygen) system, J. Phase Equilibria. 13 (2) (1992) 137-142.
- [132] M. Huš, A. Hellman, Dipole effect on ethylene epoxidation: Influence of alkali metals and chlorine, J. Catal. 363 (2018) 18–25.

- [133] W.X. Li, C. Stampfl, M. Scheffler, Insights into the function of silver as an oxidation catalyst by ab initio atomistic thermodynamics, Phys. Rev. B Condens. Matter Mater. Phys. 68 (2003) 1–15.
- [134] M Pascal, C.L.A Lamont, P Baumgärtel, R Terborg, J.T Hoeft, O Schaff, M Polcik, A.M Bradshaw, R.L Toomes, D.P Woodruff, Photoelectron diffraction study of the Ag(110)-(2×1)-O reconstruction, Surf. Sci. 464 (2-3) (2000) 83–90.
- [135] G. Dorenbos, D.O. Boerma, The structure of the Ag(110)-c(6 × 2)O surface determined with LEIS, Surf. Sci. 287-288 (1993) 443-447.
- [136] I. Costina, M. Schmid, H. Schiechl, M. Gajdoš, A. Štierle, S. Kumaragurubaran, J. Hafner, H. Dosch, P. Varga, Combined STM, LEED and DFT study of Ag(1 0 0) exposed to oxygen near atmospheric pressures, Surf. Sci. 600 (3) (2006) 617–624.
- [137] Wei-Xue Li, Catherine Stampfl, Matthias Scheffler, Oxygen adsorption on Ag (111): A density-functional theory investigation, Phys. Rev. B Condens. Matter Mater. Phys. 65 (7) (2002).
- [138] M. Gajdoš, A. Eichler, J. Hafner, Ab initio density functional study of O on the Ag(001) surface, Surf. Sci. 531 (3) (2003) 272–286.
- [139] A.F. Carley, P.R. Davies, M.W. Roberts, K.K. Thomas, Transient oxygen states in catalysis: ammonia oxidation at Ag(111), Langmuir ACS J. Surf. Colloids. 26 (2010) 16221–16225.

- [140] A.F. Carley, P.R. Davies, M.W. Roberts, K.K. Thomas, Hydroxylation of molecularly adsorbed water at Ag(111) and Cu(100) surfaces by dioxygen: photoelectron and vibrational spectroscopic studies, Surf. Sci. 238 (1990) L467–L472.
- [141] P.D. Nolan, B.R. Lutz, P.L. Tanaka, J.E. Davis, C.B. Mullins, Molecularly chemisorbed intermediates to oxygen adsorption on Pt(111): A molecular beam and electron energy-loss spectroscopy study, J. Chem. Phys. 111 (1999) 3696–3704.
- [142] K. Gustafsson, S. Andersson, Infrared spectroscopy of physisorbed and chemisorbed O2 on Pt(111), J. Chem. Phys. 120 (16) (2004) 7750–7754.
- [143] M.-L. Bocquet, D. Loffreda, Ethene Epoxidation Selectivity Inhibited by Twisted Oxametallacycle: A DFT Study on Ag Surface-Oxide, J. Am. Chem. Soc. 127 (2005) 17207–17215.
- [144] A Michaelides, M.-L Bocquet, P Sautet, A Alavi, D.A King, Structures and thermodynamic phase transitions for oxygen and silver oxide phases on Ag {111}, Chem. Phys. Lett. 367 (3-4) (2003) 344–350.
- [145] R.B. Grant, R.M. Lambert, Basic studies of the oxygen surface chemistry of silver: Chemisorbed atomic and molecular species on pure Ag(111), Surf. Sci. 146 (1984) 256–268.